

Magic configurations in Moiré Superlattice of Bilayer Photonic crystal: Almost-Perfect Flatbands and Unconventional Localization

Dung Xuan Nguyen^{1,*}, Xavier Letartre², Emmanuel Drouard², Pierre Viktorovitch², H. Chau Nguyen³, and Hai Son Nguyen^{2,4†}

¹*Brown Theoretical Physics Center and Department of Physics,*

Brown University, 182 Hope Street, Providence, Rhode Island 02912, USA

²*Univ Lyon, Ecole Centrale de Lyon, CNRS, INSA Lyon, Université Claude Bernard Lyon 1, CPE Lyon, CNRS, INL, UMR5270, 69130 Ecully, France*

³*Naturwissenschaftlich-Technische Fakultät, Universität Siegen, Walter-Flex-Straße 3, 57068 Siegen, Germany and*

⁴*Institut Universitaire de France (IUF)*

(Dated: June 14, 2021)

We investigate the physics of photonic band structures of the moiré patterns that emerged when overlapping two uni-dimensional (1D) photonic crystal slabs with mismatched periods. The band structure of our system is a result of the interplay between intra-layer and inter-layer coupling mechanisms, which can be fine-tuned via the distance separating the two layers. We derive an effective Hamiltonian that captures the essential physics of the system and reproduces all numerical simulations of electromagnetic solutions with high accuracy. Most interestingly, *magic distances* corresponding to the emergence of photonic flatbands within the whole Brillouin zone of the moiré superlattice are observed. We demonstrate that these flatband modes are tightly localized within a moiré period. Moreover, we suggest a single-band tight-binding model that describes the moiré minibands, of which the tunnelling rate can be continuously tuned via the inter-layer strength. Our results show that the band structure of bilayer photonic moiré can be engineered in the same fashion as the electronic/excitonic counterparts. It would pave the way to study many-body physics at photonic moiré flatbands and novel optoelectronic devices.

Moiré structures have been of central interest in fundamental physics during the last few years. The most important milestone is the discovery of flatbands in the moiré patterns emerged when two graphene layers are overlapped at certain *magic* twisted angles[1–3], leading to non-conventional superconductivity[4–6] and strongly correlating insulator states with nontrivial-topology[7, 8]. Motivated by the electronic *magic angles*, photonic moiré has attracted tremendous research in light of shaping novel optical phenomena. Hu *et al.* have demonstrated [9, 10] the topological transition of photonic dispersion in twisted 2D materials. However, the operating wavelength in these pioneering works are much larger than the moiré period, thus dispersion engineering is based on the anisotropy of an effective medium rather than the microscopic moiré pattern. On the other hand, Ye’s group has recently reported on the realization of 2D photonic moiré superlattice[11]. Nevertheless, this work only focused on light scattering through the moiré pattern, but the lattice is on the same plane, and there is no bi-layer, neither twisting concepts. Most recently, numerical[12] and tight-binding[13] method have been proposed to investigate twisted bilayer photonic crystal slabs. In particular, Dong *et al.* has showed that local flatband would be achieved[13] in twisted bilayer photonic crystal at small twisted angle..

In this work, we report on a theoretical study of photonic band structures in moiré patterns that emerged when two mismatched 1D subwavelength photonic crystal slabs are overlapped. The essential physics of the system can be captured by an effective four-component Hamiltonian. Accompanying the analytical theory, numerical electromagnetic simulations are performed with a case study of silicon structures operating at telecom wavelength. The obtained band structure are resulted from an interplay between intra-layer and inter-layer coupling

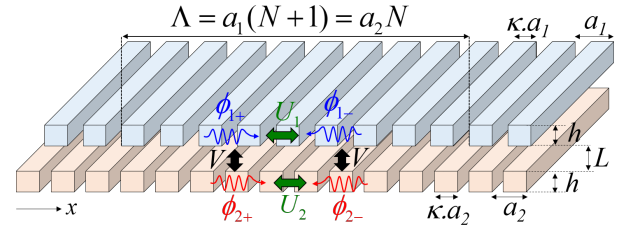


Figure 1. Moiré superlattice of two gratings with of periods a_1 and a_2 satisfying $a_1/a_2 = N/(N + 1)$.

mechanisms which is tuned via the distance separating the two layers. Importantly, *magic distances* corresponding to the emergence of photonic flatbands within the whole Brillouin zone are demonstrated. The minibands of moiré superlattice can be described by a single-band tight-binding model with Wannier functions tightly confined within a moiré period. The tunnelling rate of light between nearest neighbor Wannier states is continuously modulated by the inter-layer distance and vanished at *magic distance*, leading to flatband formation and photonic localization. Despite its simplicity, this 1D setup captures much interesting physics of moiré systems of twisted two-dimensional materials. Our findings suggest that moiré photonic is a promising strategy to engineer photonic band-structure for fundamental research and optoelectronic devices.

Our system consists of two 1D photonic crystal slabs which are two subwavelength high refractive index contrast gratings (Fig 1). These gratings have the same subwavelength thickness h and filling fraction κ and are separated by only a subwavelength distance L . Their periods a_1 and a_2 are slightly different but satisfying the commensurate condition

$a_1/a_2 = N/(N + 1)$ for a natural number N . The period of the superlattice is given by $\Lambda = (N + 1)a_1 = Na_2$, consisting of $N + 1$ periods of the upper grating and N period of the lower one. In the regime of $N \gg 1$, a *semi-continuous approach* can be implemented: the two gratings are almost identical and the *moiré pattern* corresponds to a continuous shifting function $\delta(x)$ of the upper grating with respect to the lower grating, given by $\delta(0 \leq x \leq \Lambda) = x/N$. The shifting δ sweeps an amount $a_0 = (a_1 + a_2)/2$ when x varies across a moiré period. In other word, the moiré superlattice is obtained from the bilayer lattice by introducing a slight period mismatch: the period of the upper grating is shrunken from a_0 to a_1 and the period of the lower one is stretched from a_0 to a_2 . This configuration leads to a modulated relative displacement $\delta(x)$ with respect to the coordinate x . Two special configurations of $\delta/a_0 = 0$ and 0.5 are referred to as *AA-* and *AB-*stackings, resembling the terminology in Bilayer Graphene structure [14]. The moiré pattern is a period of a superlattice made of bilayer structures varying continuously from AA stacking to AB stacking. The period mismatch leads to a Brillouin zone mismatch and the size of the mini Brillouin zone K_M is given by $K_M = K_1 - K_2$, where $K_1 = 2\pi/a_1$ and $K_2 = 2\pi/a_2$.

In our perturbation approach, the dispersion characteristic of the moiré superlattice is derived from two coupling mechanisms among forward (ϕ_{1+}, ϕ_{2+}) and backward (ϕ_{1-}, ϕ_{2-}) fundamental guided waves of the two noncorrugated slabs with effective refractive index: *i) Intra-layer coupling* due to the diffractive processes[15] between counter-propagating waves from the same layer. *ii) Inter-layer coupling* via evanescence between co-propagating waves from separated layers. Using ($\phi_{1+}, \phi_{1-}, \phi_{2+}, \phi_{2-}$) as basis, eigenmodes of the system are described by the following Hamiltonian (detailed derivation is given in the Supplemental Material):

$$H = \begin{pmatrix} -iv\partial_x + \omega_1 & U_1 & V & 0 \\ U_1 & iv\partial_x + \omega_1 & 0 & V \\ V & 0 & -iv\partial_x + \omega_2 & U_2 e^{-iK_M x} \\ 0 & V & U_2 e^{iK_M x} & iv\partial_x + \omega_2 \end{pmatrix} \quad (1)$$

Here $U_{1,2}$ are the intra-layer coupling rates and V is the inter-layer one; v and $\omega_{1,2}$ are the group velocity and offset energy of the guided waves at the Brillouin zone edge for each grating. A slight difference of values of the offset pulsation and the intra-layer coupling strength for each grating are due to the period mismatch, with $\omega_1 \approx \omega_2 \approx \omega_0$ and $U_1 \approx U_2 \approx U$ where ω_0 and U are the offset pulsation and the intra-layer coupling strength in the grating of period a_0 .

The energy-momentum dispersion is simulated numerically using Rigorous Coupled-Wave Analysis (RCWA) method [16–18]. The numerical results corresponding to $N = 13$ when increasing the separation distance L are presented in figures 2a-e. When L is comparable to a_0 , the band structure is simply the folding of single layer dispersions (Fig 2a). It suggests that the inter-layer coupling mechanism is negligible with respect to the intra-layer ones (i.e. $V \ll U$) for $L \gtrsim a_0$.

In this configuration, a bandgap, purely due to the intra-layer coupling mechanism, is observed (Fig 2a). In analogy to semiconductor terminology, we refer to these upper/lower bands as *conduction-like/valence-like*. When $L \lesssim a_0$, the band hybridization due to the inter-layer coupling results in the formation of a pair of particle-hole minibands, referred to as electron-like/hole-like moiré band (Figs 2b-e). These two bands emerge within the bandgap of uncoupled layers and are well isolated from the conduction/valence-like continuum. In the following, we will pay particular attention to the behavior of these two bands when tuning the inter-layer interaction. One may note that with the choice of $a_0 = 300 \text{ nm}$, the spectral range of these band is in the telecom (i.e. $\sim 1.5 \mu\text{m}$). Intriguingly, there are some specific values of L at which the bandwidth of these bands becomes almost zero, and these moiré bands are nearly perfectly flat. Figures 2c and 2d depict the band structures with flat hole-like moiré band, and almost-flat electron-like band. Inspired by the analogy with the appearance of flatbands at magic angles in twisted bilayer graphene [2], we called these values *magic distances*. The moiré band structure is calculated using the Hamiltonian model given by Eq. (1), taking v, U, ω_0 and V as input parameters. These parameters are retrieved from the simulation of single and bilayer lattice[19, 20]. Figures 2f-j depict the band structures obtained by analytical calculations. These results reproduce quantitatively the numerical results presented in Figs 2a-e, showing the emergence of moiré states within the bandgap and their flattening at magic distances. Noticeably, there is a slight difference between simulation and analytical results: the RCWA suggest that the flattening of the electron-like band always takes place at a slightly smaller distance L than the one of the hole-like band, while the Hamiltonian model predicts that both bands become flat almost simultaneously.

The *global spectral bandwidth*, defined as $\Delta\omega = \max_q(\omega) - \min_q(\omega)$, is used as the figure of merit to evaluate the flatness of moiré minibands. Figures 3a-c depict the global spectral bandwidth of the hole-like moiré band if different moiré superlattice ($N = 9, 13$ and 19) when scanning L . These results confirm the existence of magic distances, corresponding to the bandwidth vanishings. All of the analytical calculations are obtained with the same set of parameters that are previously presented. We highlight that the Hamiltonian model provides almost perfectly both the number of magic distances and its values.

For each moiré superlattice (i.e. a given N), our design exhibits two adjustable parameters: *i)* The distance L for tuning the inter-layer coupling V ($V = V_0$ when $L = 0$ and decreasing exponentially when increasing L [20]); *ii)* The filling fraction κ , defined in Fig.1, for tuning the intra-layer coupling U ($U = 0$ when $\kappa = 1$ and increasing when decreasing κ [20]). Up to now, we have been investigating flatband emergence by scanning L while fixing $\kappa = 0.8$ (i.e. $U = U_0$). However, the direct parameters of the Hamiltonian (1) are U, V and N (from K_M). Thus a complete picture of magic configuration is captured when varying both V/U (i.e. competition

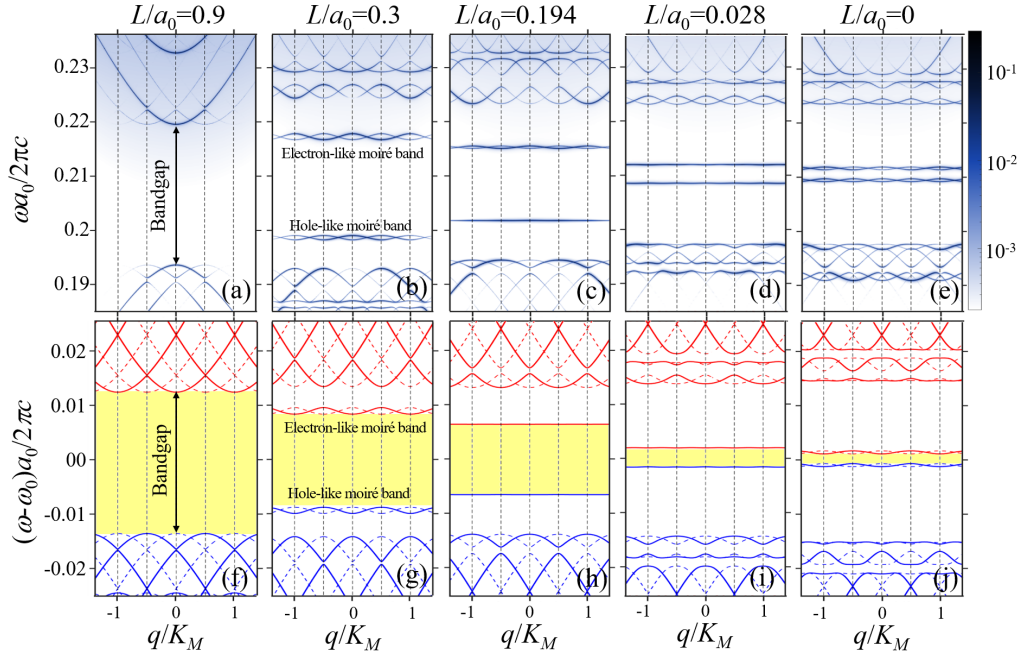


Figure 2. (a-e) Simulated band structures corresponding to different L values. The design for the simulation uses silicon ($n = 3.54$) as the grating material, with $h = 180 \text{ nm}$, $\kappa = 0.8$, $a_0 = (a_1 + a_2)/2 = 300 \text{ nm}$ and $N = 13$. The photonic modes of uncoupled gratings are located below the light-line and the inter-layer coupling mechanisms, if not strong enough, would not be able to make these modes accessible for RCWA simulations. To solve this, a double period perturbation of 5% is implemented for the design of each grating. The unit-cell in RCWA simulation consists of two moiré patterns: One is shrunken to 0.95Λ , and the other one is dilated to 1.05Λ . (f-i) Calculations using the effective Hamiltonian of band structures shown in (a-e). To compare with the RCWA simulations having double period perturbation, dash-lines have been added, indicating the folding of the band structure.

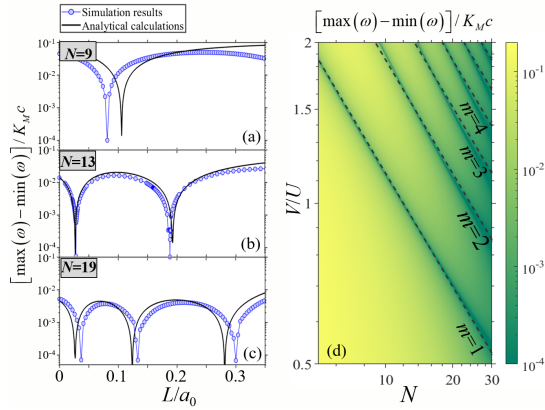


Figure 3. (a-c) The global spectral bandwidth of the hole-like moiré band as a function of L for different moiré patterns. Blue circles are results from RCWA simulations. Black lines are analytical calculations. (d) The global spectral bandwidth as a function of V/U and N , with $U = U_0$. The dashed lines correspond to the empirical law (2).

between inter versus intralayer coupling) and N (i.e. moiré pattern). Figure 3d presents the global bandwidth when scanning N and V/U within a reasonable range [21]. The observed “resonant dips” correspond to different magic configurations.

Dimensional analysis of Hamiltonian (1) suggests that our system is driven by two dimensionless ratios V/U , and $U/K_M \sim NU$ [20]. Indeed, fitting the resonances of Fig.3d by a power law, we obtain a very simple empirical relation between these two dimensionless parameters:

$$N_m U = m \times \eta \times \left(\frac{V}{U}\right)^\gamma, \quad m = 1, 2, 3, \dots \quad (2)$$

with the $\gamma \approx -1.42$, $\eta \approx 12U_0$, and m is the counting order of the magic configuration. We note that N is the “moiré parameter” in our system and playing the same role as the twist angle in twisted bilayer graphene (each value of moiré parameter defines a moiré pattern)[22, 23]. Therefore, the good metric for magic configurations is the magic number N_m , and Eq. (2) provides the design rule to achieve them. The analogy and similitude between this law and the one for magic angles in twisted bi-layer graphene [2] are striking and we expect an appealing interpretation for this simple relation.

Knowing that flatband states would give rise to an unconventional localization regime [11, 27, 28], we now investigate the localization of light at magic configurations. A closer look at the two moiré bands in Figs. 2 reveals that their dispersion characteristic are nearly single harmonic functions with the dominance of the first Fourier component with respect to higher-orders. Consequently, this suggests

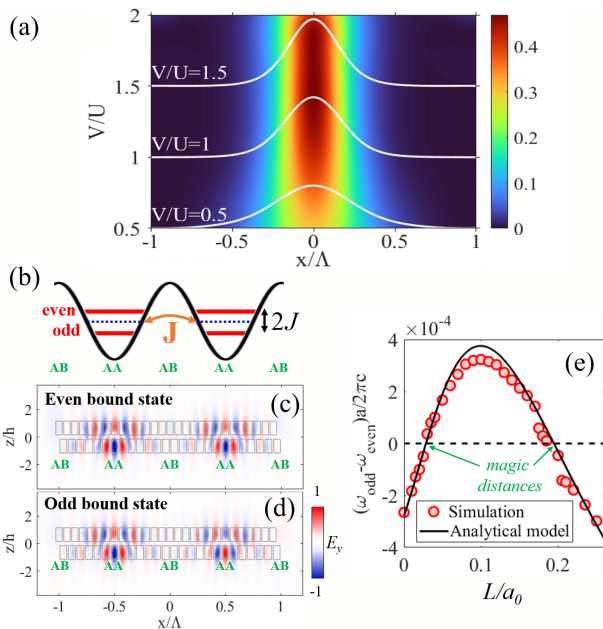


Figure 4. (a) Wannier function, calculated by the twisted parallel transport gauge [24], of the hole-like moiré band when scanning the V/U ratio. (b) Sketch of a hole-like “diatomic molecule” made of two moiré cells. (c,d) The field distribution of the two hole-like bound states obtained by Finite-difference time-domain (FDTD) simulations. The chosen moiré design is the same as the one in RCWA simulations in Fig. 2. (e) The energy splitting between the two bound states as a function of L . Red circles are results from FDTD simulations, and the solid black line is the result from the effective Hamiltonian. For the analytical calculation, the boundary condition is chosen so that outside of the moiré molecule is bilayer structure of AB sites, and the bound states are calculated by the transfer matrix method [25, 26]. For FDTD simulations, the structure only consists of two moiré cells.

that each moiré band may be described by a textbook single-band tight-binding model with only a few nearest neighbour couplings taken into account. It is of interest to compute the Wannier functions for the band under consideration since Wannier functions are the natural basis for the tight-binding model [29]. Figure 4(a) depicts the result of this calculation when scanning the ratio V/U , showing that more than 94% of the Wannier density is located within a single moiré cell. Such a concentration confirms the use of this Wannier function as a pseudo-orbital wave function for the tight-binding model with nearest neighbour couplings. However, it is important to stress that the high concentration of the Wannier function is not necessarily related to flatband formations. Yet, the physics of the moiré bands can be captured quite well by a simple tight-binding scheme in the Wannier basis. In this scenario, the moiré superlattice engenders a periodic potential landscape with minima at AA sites. Trapped photons in the Wannier states can tunnel to the nearest neighbour ones with tunnelling rate J to form moiré bands of bandwidth $2|J|$. As consequence, when the couple $(NU, V/U)$ satisfies the Eq. (2)

of magic configurations, the only way to obtain dispersionless bands is that the effective tunneling rate J becomes zero. This leads to the tightly localization of light within a single moiré cell at magic configurations. The compact localized states [30] of our localization is simply the Wannier function. We notice a resemblance of the flatband emergence in our system compared to the one in twisted bilayer graphene system [2, 31, 32]: both correspond to the good localization at the AA sites.

Keeping in mind the ability to localize light to a moiré period with high quality (albeit non-perfect), we investigate a much simpler problem: a “diatomic molecule” made of two moiré cells (Fig. 4b). Figures 4c,d depicts the field distribution of the hole-like bound states with even (Fig. 4c) and odd (Fig. 4d) parity regarding the lateral mirror symmetry. The energy splitting when scanning the distance L is presented in Fig. 4e. Again, the results from the analytical model and numerical simulations show a very good agreement. Notably, these results demonstrate the crossing of these bound states exactly at the magic distances of the moiré superlattice from Fig. 3b. Consequently, it supports that the tunnelling rate J changes sign when scanning L across a magic distance value and vanishes when L takes a magic distance value.

In conclusion, we have investigated theoretically the 1D moiré superlattice of bilayer photonic crystal. All of analytical results derived from a simple effective Hamiltonian are in good agreement with numerical simulations, showing the emergence of flatband at magic configurations. The conditions for flatbands unify to a nontrivial relation between the counting order of the magic configuration and the magic number, given by $N_m \sim m$. The physics of the moiré minibands is captured by a simple tight-binding model, resulting in localization of photonic states within a single moiré period at flatband configurations when the tunnelling rate vanishes accidentally. As fundamental perspective, the implementation of nonlinearity via Kerr nonlinearity [33] or exciton-polariton platform [34], would pave the way to investigate the strongly correlated bosonic flatband physics [35–37] with intriguing phases of 1D matters [38]. For applications in optoelectronic devices, the design in this work uses silicon as dielectric material, operating in the telecom range with feasible fabrication [19, 39, 40], and is transferable to 1D integrated optics. The high sensitivity of dispersion band structure to the refractive index of surrounding medium (which determines the parameter U) and spacing medium (which determines the parameter V) can be harnessed for applications in sensing. Furthermore, the localization of light within the moiré period also suggests a unique way to engineer lattice of resonators of a high-quality factor for a phase-locked micro-laser array or high Purcell factor for tailoring spontaneous emission of quantum emitters. Another realization scheme is with dual-core fiber Bragg gratings [41, 42] to study soliton physics arising from photonic nonlinearity which will be greatly enhanced at flatband configurations [41–43].

Acknowledgement: The authors thank Stephen Carr, Nguyen Viet Hung, and Steven H. Simon for fruitful discussions. The work is partly funded by the French National Re-

search Agency (ANR) under the project POPEYE (ANR-17-CE24-0020) and the IDEXLYON from Université de Lyon, Scientific Breakthrough project TORE within the Programme Investissements d’Avenir (ANR-19-IDEX-0005). DXN was supported by Brown Theoretical Physics Center. HCN was supported by the Deutsche Forschungsgemeinschaft (DFG, German Research Foundation, project numbers 447948357 and 440958198), the Sino-German Center for Research Promotion (Project M-0294), and the ERC (Consolidator Grant 683107/TempoQ). RCWA simulations were performed on the CNRS/IN2P3 Computing Center in Lyon.

* dung_x_nguyen@brown.edu

† hai_son.nguyen@ec-lyon.fr

- [1] R. Bistritzer and A. H. MacDonald, Moiré bands in twisted double-layer graphene, *Proceedings of the National Academy of Sciences* **108**, 12233 (2011), <https://www.pnas.org/content/108/30/12233.full.pdf>.
- [2] G. Tarnopolsky, A. J. Kruchkov, and A. Vishwanath, Origin of Magic Angles in Twisted Bilayer Graphene, *Phys. Rev. Lett.* **122**, 106405 (2019).
- [3] S. Lisi, X. Lu, T. Benschop, T. A. de Jong, P. Stepanov, J. R. Duran, F. Margot, I. Cucchi, E. Cappelli, A. Hunter, A. Tamai, V. Kandyba, A. Giampietri, A. Barinov, J. Jobst, V. Stalman, M. Leeuwenhoek, K. Watanabe, T. Taniguchi, L. Rademaker, S. J. van der Molen, M. P. Allan, D. K. Efetov, and F. Baumberger, Observation of flat bands in twisted bilayer graphene, *Nature Physics* **17**, 189 (2021).
- [4] Y. Cao, V. Fatemi, S. Fang, K. Watanabe, T. Taniguchi, E. Kaxiras, and P. Jarillo-Herrero, Unconventional superconductivity in magic-angle graphene superlattices, *Nature* **556**, 43 (2018).
- [5] H. S. Arora, R. Polski, Y. Zhang, A. Thomson, Y. Choi, H. Kim, Z. Lin, I. Z. Wilson, X. Xu, J.-H. Chu, K. Watanabe, T. Taniguchi, J. Alicea, and S. Nadj-Perge, Superconductivity in metallic twisted bilayer graphene stabilized by WSe₂, *Nature* **583**, 379 (2020).
- [6] P. Stepanov, I. Das, X. Lu, A. Fahimniya, K. Watanabe, T. Taniguchi, F. H. L. Koppens, J. Lischner, L. Levitov, and D. K. Efetov, Untying the insulating and superconducting orders in magic-angle graphene, *Nature* **583**, 375 (2020).
- [7] Z. Song, Z. Wang, W. Shi, G. Li, C. Fang, and B. A. Bernevig, All magic angles in twisted bilayer graphene are topological, *Phys. Rev. Lett.* **123**, 036401 (2019).
- [8] S. Wu, Z. Zhang, K. Watanabe, T. Taniguchi, and E. Y. Andrei, Chern insulators and topological flat-bands in magic-angle twisted bilayer graphene (2020), [arXiv:2007.03735](https://arxiv.org/abs/2007.03735) [cond-mat.mes-hall].
- [9] G. Hu, Q. Ou, G. Si, Y. Wu, J. Wu, Z. Dai, A. Krasnok, Y. Mazor, Q. Zhang, Q. Bao, C. W. Qiu, and A. Alù, Topological polaritons and photonic magic angles in twisted α -MoO₃ bilayers, *Nature* **582**, 209 (2020).
- [10] G. Hu, A. Krasnok, Y. Mazor, C. W. Qiu, and A. Alù, Moiré Hyperbolic Metasurfaces, *Nano Letters* **20**, 3217 (2020).
- [11] P. Wang, Y. Zheng, X. Chen, C. Huang, Y. V. Kartashov, L. Torner, V. V. Konotop, and F. Ye, Localization and delocalization of light in photonic moiré lattices, *Nature* **577**, 42 (2020).
- [12] B. Lou, N. Zhao, M. Minkov, C. Guo, M. Orenstein, and S. Fan, Theory for Twisted Bilayer Photonic Crystal Slabs, *Physical Review Letters* **126**, 136101 (2021).
- [13] K. Dong, T. Zhang, J. Li, Q. Wang, F. Yang, Y. Rho, D. Wang, C. P. Grigoropoulos, J. Wu, and J. Yao, Flat bands in magic-angle bilayer photonic crystals at small twists, *Phys. Rev. Lett.* **126**, 223601 (2021).
- [14] A. V. Rozhkov, A. O. Sboychakov, A. L. Rakhmanov, and F. Nori, Electronic properties of graphene-based bilayer systems, *Physics Reports* **648**, 1 (2016), [arXiv:1511.06706](https://arxiv.org/abs/1511.06706).
- [15] K. Okamoto, Chapter 4 - coupled mode theory, in *Fundamentals of Optical Waveguides (Second Edition)*, edited by K. Okamoto (Academic Press, Burlington, 2006) second edition ed., pp. 159–207.
- [16] M. G. Moharam and T. K. Gaylord, Rigorous coupled-wave analysis of metallic surface-relief gratings, *J. Opt. Soc. Am. A* **3**, 1780 (1986).
- [17] V. Liu and S. Fan, S4 : A free electromagnetic solver for layered periodic structures, *Computer Physics Communications* **183**, 2233 (2012).
- [18] D. Alonso-Álvarez, T. Wilson, P. Pearce, M. Führer, D. Farrell, and N. Ekins-Daukes, Solcore: a multi-scale, python-based library for modelling solar cells and semiconductor materials, *Journal of Computational Electronics* **17**, 1099 (2018).
- [19] H. Nguyen, F. Dubois, T. Deschamps, S. Cuffe, A. Pardon, J.-L. Leclercq, C. Seassal, X. Letartre, and P. Viktorovitch, Symmetry breaking in photonic crystals: On-demand dispersion from flatband to dirac cones, *Physical Review Letters* **120**, 10.1103/physrevlett.120.066102 (2018).
- [20] See Supplemental Materials at (link) for full derivation details of the Hamiltonian models, the numerical simulations and parameter retrievals from band structure of single layer and bilayer lattices, as well as other further details.
- [21] N is varied from 5 to 30 (If N is too small, the continuum model is not valid. If N is too big, the Brillouin zone becomes too small and bands are naturally very flat). V/U is varied from 0.5 to 2 (If V/U is too small, the approximation $L \ll a_0$ is not valid. If $V/U > 2$, the two moiré bands merge[20]).
- [22] J. M. B. Lopes dos Santos, N. M. R. Peres, and A. H. Castro Neto, Graphene bilayer with a twist: Electronic structure, *Phys. Rev. Lett.* **99**, 256802 (2007).
- [23] J. M. B. Lopes dos Santos, N. M. R. Peres, and A. H. Castro Neto, Continuum model of the twisted graphene bilayer, *Phys. Rev. B* **86**, 155449 (2012).
- [24] D. Vanderbilt, *Berry phases in electronic structure theory* (Cambridge University Press, 2018).
- [25] J. H. Davies, *The physics of low-dimensional semiconductors: an introduction* (Cambridge University Press, 1998).
- [26] H. C. Nguyen, M. T. Hoang, and V. L. Nguyen, Quasi-bound states induced by one-dimensional potentials in graphene, *Phys. Rev. B* **79**, 035411 (2009).
- [27] S. Mukherjee, A. Spracklen, D. Choudhury, N. Goldman, P. Öhberg, E. Andersson, and R. R. Thomson, Observation of a localized flat-band state in a photonic lieb lattice, *Phys. Rev. Lett.* **114**, 245504 (2015).
- [28] R. A. Vicencio, C. Cantillano, L. Morales-Inostroza, B. Real, C. Mejía-Cortés, S. Weimann, A. Szameit, and M. I. Molina, Observation of localized states in lieb photonic lattices, *Phys. Rev. Lett.* **114**, 245503 (2015).
- [29] N. W. Ashcroft and N. D. Mermin, *Solid State Physics* (Holt-Saunders, 1976).
- [30] W. Maimaiti, A. Andreanov, H. C. Park, O. Gendelman, and S. Flach, Compact localized states and flat-band generators in one dimension, *Phys. Rev. B* **95**, 115135 (2017).
- [31] A. C. Gadelha, D. A. A. Ohlberg, C. Rabelo, E. G. S. Neto, T. L. Vasconcelos, J. L. Campos, J. S. Lemos, V. Ornelas, D. Mi-

- randa, R. Nadas, F. C. Santana, K. Watanabe, T. Taniguchi, B. van Troeye, M. Lamparski, V. Meunier, V.-H. Nguyen, D. Paszko, J.-C. Charlier, L. C. Campos, L. G. Cançado, G. Medeiros-Ribeiro, and A. Jorio, Localization of lattice dynamics in low-angle twisted bilayer graphene, *Nature* **590**, 405 (2021).
- [32] V. H. Nguyen, D. Paszko, M. Lamparski, B. V. Troeye, V. Meunier, and J. C. Charlier, Electronic localization in small-angle twisted bilayer graphene (2021), [arXiv:2102.05376](https://arxiv.org/abs/2102.05376) [cond-mat.mes-hall].
- [33] D. Rivas and M. I. Molina, Seltrapping in flat band lattices with nonlinear disorder, *Scientific Reports* **10**, 5229 (2020).
- [34] V. Goblot, B. Rauer, F. Vicentini, A. Le Boité, E. Galopin, A. Lemaître, L. Le Gratiet, A. Harouri, I. Sagnes, S. Ravets, C. Ciuti, A. Amo, and J. Bloch, Nonlinear polariton fluids in a flatband reveal discrete gap solitons, *Phys. Rev. Lett.* **123**, 113901 (2019).
- [35] D. Leykam, J. D. Bodyfelt, A. S. Desyatnikov, and S. Flach, Localization of weakly disordered flat band states, *The European Physical Journal B* **90**, 1 (2017).
- [36] C. Danieli, A. Andreanov, and S. Flach, Many-body flatband localization, *Phys. Rev. B* **102**, 041116 (2020).
- [37] E. Khalaf, S. Chatterjee, N. Bultinck, M. P. Zaletel, and A. Vishwanath, Charged skyrmions and topological origin of superconductivity in magic angle graphene (2021), [arXiv:2004.00638](https://arxiv.org/abs/2004.00638) [cond-mat.str-el].
- [38] T. Giamarchi, *Quantum Physics in One Dimension* (Oxford University Press, 2003).
- [39] Y. Shuai, D. Zhao, Y. Liu, C. Stambaugh, J. Lawall, and W. Zhou, Coupled bilayer photonic crystal slab electro-optic spatial light modulators, *IEEE Photonics Journal* **9**, 1 (2017).
- [40] S. Cuffe, F. Dubois, M. S. R. Huang, D. Li, R. Zia, X. Letartre, P. Viktorovitch, and H. S. Nguyen, Tailoring the local density of optical states and directionality of light emission by symmetry breaking, *IEEE Journal of Selected Topics in Quantum Electronics* **25**, 1 (2019).
- [41] W. C. K. Mak, P. L. Chu, and B. A. Malomed, Solitary waves in coupled nonlinear waveguides with bragg gratings, *J. Opt. Soc. Am. B* **15**, 1685 (1998).
- [42] T. Ahmed and J. Atai, Soliton-soliton dynamics in a dual-core system with separated nonlinearity and nonuniform Bragg grating, *Nonlinear Dynamics* **97**, 1515 (2019).
- [43] B. J. Eggleton, R. E. Slusher, C. M. de Sterke, P. A. Krug, and J. E. Sipe, Bragg grating solitons, *Phys. Rev. Lett.* **76**, 1627 (1996).
- [44] Here, we ignore the coupling between the positive (negative) mode on the upper layer and the negative (positive) mode on the lower layer. This coupling includes a fast oscillation factor due to the fact that the positive mode and the negative mode have different wave vectors.
- [45] This can be demonstrated by using $\sigma_z \sigma_{\pm} \sigma_z^{\dagger} = -\sigma_{\pm}$ and $T_{\Lambda} e^{-i\theta \sigma_z} T_{\Lambda}^{\dagger} = -e^{-i\theta \sigma_z}$.
- [46] C. Rackauckas and Q. Nie, Differentialequations.jl—a performant and feature-rich ecosystem for solving differential equations in julia, *Journal of Open Research Software* **5** (2017).

— Supplementary Material —
**Magic configurations in Moiré Superlattice of Bilayer Photonic crystal:
 Almost-Perfect Flatbands and Unconventional Localization**

Dung Xuan Nguyen, Xavier Letartre, Emmanuel Drouard, Pierre Viktorovitch, H Chau Nguyen, Hai Son Nguyen

AB INITIO DERIVATION OF MOIRÉ LATTICE HAMILTONIAN

In this section, we provide the detailed derivation of the effective Hamiltonian in the main text.

Hamiltonian of a single grating wave-guide

Wave function a single grating wave-guide

In perturbation theory, the eigenmodes in photonic grating are constituted by the coupling between forward $\varphi_+(k \geq 0)$ and backward $\varphi_-(k \leq 0)$ propagating waves of the non-corrugated waveguide of effective refractive index (see Fig S1a). Here the *wave-function* φ corresponds to the electric field E_y for TE modes, and the magnetic field H_y for TM modes. The dispersion characteristic $\omega_+(k \geq 0)$ and $\omega_-(k \leq 0)$, $\omega_+(k) = \omega_-(-k)$, of these guided modes lies below the light-line (see Fig S1b) and are obtained by solving Maxwell equations of planar waveguide with effective refractive index. We can extend the definition of positive and negative wavefunctions for any k value by replacing $\varphi_{\pm}(k)$ by $\Phi_{\pm}(k)$, given by:

$$\Phi_{\pm}(k) = \Theta(\pm k)\varphi_{\pm}(k), \quad (\text{S1})$$

where Θ is the Heaviside function, $\theta(x) = 1$ if $x \geq 0$ and $\theta(x) = 0$ if $x < 0$. With such definition, the spatial wave-function $\Phi_{\pm}(x)$ of positive and negative modes is obtained by the Fourier transform of $\Phi_{\pm}(k)$:

$$\Phi_{\pm}(x) = \int \frac{dk}{2\pi} \Phi_{\pm}(k)e^{ikx}. \quad (\text{S2})$$

With a spatial period a , the reciprocal lattice vector is given by $K_0 = \frac{2\pi}{a_0}$. High symmetry points in the momentum space are at wavevectors $\frac{lK_0}{2}$ with $l \in \mathbb{Z}$. A given odd(even) value of l corresponds to a $X(\Gamma)$ point of the BZs. The *effective* wave-functions of positive (negative mode) near the high symmetry point $\frac{lK_0}{2}$ ($-\frac{lK_0}{2}$) are defined by:

$$\Phi_{l,\pm}(q) = \Phi_{\pm}\left(\pm\frac{lK_0}{2} + q\right), \quad q \in \left[-\frac{K_0}{4}, \frac{K_0}{4}\right], \quad (\text{S3})$$

and

$$\Phi_{l,\pm}(x) = \int_{-\frac{K_0}{4}}^{\frac{K_0}{4}} \frac{dq}{2\pi} \Phi_{l,\pm}(q)e^{iqx}. \quad (\text{S4})$$

We verify easily the relation between $\Phi_{\pm}(x)$ and $\Phi_{l,\pm}(x)$, given by:

$$\Phi_{\pm}(x) = \sum_{l \in \mathbb{Z}} e^{\pm i\frac{lK_0}{2}x} \Phi_{l,\pm}(x) \quad (\text{S5})$$

Since band structures are mostly studied in the vicinity of a high symmetry point of the BZs, the most appropriate basis in real space and momentum space given by:

$$\Psi_l(x) = \begin{pmatrix} \Phi_{l,+}(x) \\ \Phi_{l,-}(x) \end{pmatrix}. \quad (\text{S6})$$

Note that due to the fact that positive mode has positive wave-vectors and the negative mode has negative wave-vectors, only $l \in \mathbb{N}^*$ appears in the definitions (S6). In the vicinity $|q| \ll \frac{K_0}{4}$ of high symmetry points (the blue points in Fig S1b) in momentum space, these relations can be approximated by

$$\omega_+\left(\frac{lK_0}{2} + q\right) \approx \omega_{0l} + v_l q, \quad \omega_-\left(-\frac{lK_0}{2} + q\right) \approx \omega_{0l} - v_l q \quad (\text{S7})$$

We have the *effective* free Hamiltonian density in momentum space $H_{(l)}^{\text{free}}(q)$ near the high symmetry points in the momentum space

$$H_l^{\text{free}}(q) = (\omega_{0l} + v_l q) \Phi_{l,+}^\dagger(q) \Phi_{l,+}(q) + (\omega_{0l} - v_l q) \Phi_{l,-}^\dagger(q) \Phi_{l,-}(q), \quad (\text{S8})$$

Diffractive coupling between counter-propagating waves

Due to grating, the positive and the negative modes couple with each other via diffractive coupling

$$\mathcal{H}^{\text{diffrac}} = \int dx U_D(x) \Phi_+^\dagger(x) \Phi_-(x) + h.c. \quad (\text{S9})$$

where the diffractive coupling function $U_D(x)$ is periodic with period a :

$$U_D(x) = \sum_{l \in \mathbb{Z}} U_l e^{ilK_0 x}, \quad (\text{S10})$$

where $U_l = U_{-l}$ because of the C_2 symmetry (reflection $x \rightarrow -x$) of the grating. Due to the diffractive coupling, effectively, the positive mode couple with the negative mode that is shifted by lK_0 in the momentum space. Vice versa, one can think of the diffractive coupling is the negative mode couples with the positive mode that is shifted by $-lK_0$ in the momentum space. The bandgaps will be open at the *crossing points* between the positive (negative) band and the shifted negative (positive) band. The strong coupling points are $K_C^+ = \frac{lK_0}{2}$ of the positive band and $-K_C^- = -\frac{lK_0}{2}$ of the negative band. These are also the high symmetry points of the BZs. Due to the diffractive coupling mechanism, l is called *diffractive order*. We can rewrite the coupling in terms of the *effective* wave-functions defined in Eqs. (S3),(S4) and (S5):

$$\mathcal{H}^{\text{diffrac}} = \sum_{\substack{l \in \mathbb{N}^* \\ -l \leq n \leq l}} \int dx U_l \Phi_{l+n,+}^\dagger(x) \Phi_{l-n,-}(x) + h.c. \quad (\text{S11})$$

Note that since positive mode has positive wave-vectors and the negative mode has negative wave-vectors, only $l \in \mathbb{N}^*$ appears in the summation of Eq. (S11) and n runs from $-l$ to l due to momentum conservation. However, the effective coupling becomes important when the energies of positive and negative bands are approximately identical, which corresponds to $n = 0$. Hence we rewrite the diffractive Hamiltonian as:

$$\mathcal{H}^{\text{diffrac}} = \sum_{l \in \mathbb{N}^*} \int dx U_l \Phi_{l,+}^\dagger(x) \Phi_{l,-}(x) + h.c. = \sum_{l \in \mathbb{N}^*} \int \frac{dq}{2\pi} U_l \Phi_{l,+}^\dagger(q) \Phi_{l,-}(q) + h.c. \quad (\text{S12})$$

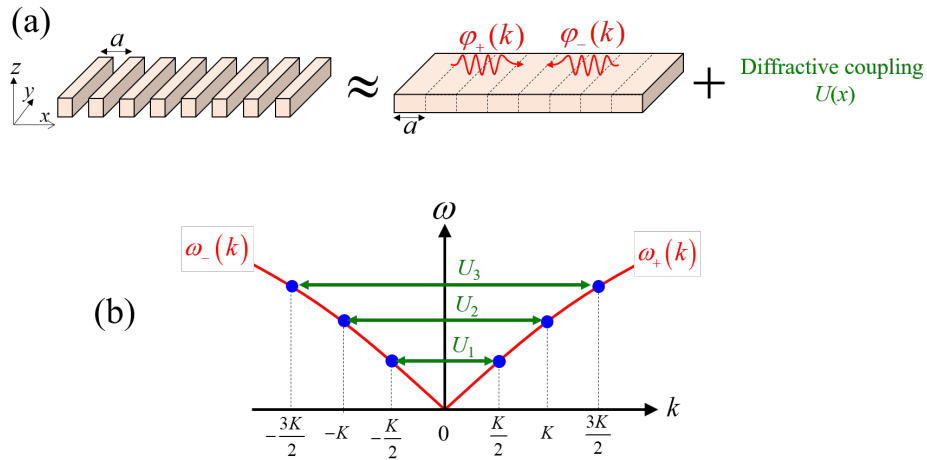


Figure S1. (a) Sketch of the photonic grating and the non-corrugated waveguide in effective refractive index approach. (b) Dispersions relation of photonic guided modes $\omega_{\pm}(k)$ and the coupling between positive and negative modes due to periodic potentials $U_D(x) = \sum_l U_l e^{i \frac{2l\pi}{a} x}$.

Combining the (S8) and the diffractive coupling (S12), we can derive the *effective* Hamiltonian near the high symmetry point in the momentum basis

$$H_{\text{single}}(q) = \mathcal{H}^{\text{free}} + \mathcal{H}^{\text{diffrac}} = \begin{pmatrix} \omega_{0l} + v_l q & U_l \\ U_l & \omega_{0l} - v_l q \end{pmatrix} \quad (\text{S13})$$

From now on, we will concentrate on the high symmetry point corresponds to $l = 1$. We then replace $\omega_{01} \rightarrow \omega_0$, $U_1 \rightarrow U$ and $v_1 \rightarrow v$, thus:

$$H_{\text{single}}(q) = \begin{pmatrix} \omega_0 + vq & U \\ U & \omega_0 - vq \end{pmatrix} \quad (\text{S14})$$

In the subsequent sections, we will omit the l indices and implicitly use Φ_{\pm} as $\Phi_{1,\pm}$ in (S4).

Effective Hamiltonian of bilayer

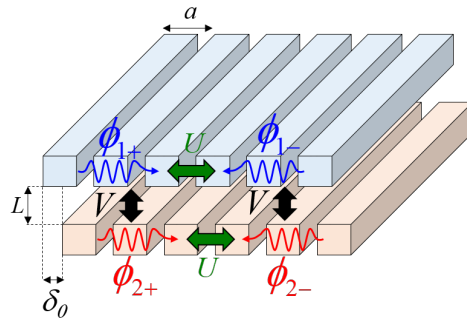


Figure S2. (a) Sketch of a bilayer grating structure.

To understand the inter-layer coupling mechanisms, an intuitive and informative example is the configuration of bilayer photonic lattice, referred to as the “fish-bone” structure in Ref [19]. Such a configuration consists of two identical gratings, one on top of the other with a relative displacement δ_0 (Fig S2). Two special configurations of $\delta_0/a_0 = 0$ and 0.5 are respectively the equivalent of *AA* and *AB* stackings in Bilayer Graphene structure [14]. We use the notation system with the implementation of index (1) and (2) to distinguish the *upper* and *lower* layer. We consider the basis made of *effective* wave-functions near the crossing point of the positive and the negative bands of each layer

$$\Psi^{(1)}(x) = \begin{pmatrix} \Phi_+^{(1)}(x) \\ \Phi_-^{(1)}(x) \end{pmatrix}, \quad \Psi^{(2)}(y) = \begin{pmatrix} \Phi_+^{(2)}(y) \\ \Phi_-^{(2)}(y) \end{pmatrix}. \quad (\text{S15})$$

Similar to the case of single layer, the Hamiltonian densities of uncoupled layers in these basis are:

$$H_{\text{single}}^{(1)}(x) = \begin{pmatrix} \omega_0 - iv\partial_x & U \\ U & \omega_0 + iv\partial_x \end{pmatrix}, \quad H_{\text{single}}^{(2)}(y) = \begin{pmatrix} \omega_0 - iv\partial_y & U \\ U & \omega_0 + iv\partial_y \end{pmatrix}. \quad (\text{S16})$$

The evanescent coupling of the bilayer configuration is [44]

$$\mathcal{H}_{\text{bilayer}}^{\text{inter}} = \int dx \int dy \left\{ \Phi_+^{(1)\dagger}(x) \Phi_+^{(2)}(y) \mathcal{V}_{\text{f-b}}(x-y) + \Phi_-^{(1)\dagger}(x) \Phi_-^{(2)}(y) \mathcal{V}_{\text{f-b}}(x-y) \right\} + h.c. \quad (\text{S17})$$

In the regime in $L \ll a$, we can assume that $\mathcal{V}_{\text{f-b}}(x-y) = V \delta(x-y-\delta_0)$. If we only consider the effective modes near the symmetry point corresponds to $l = 1$, we rewrite the inter-layer coupling Hamiltonian as:

$$\mathcal{H}_{\text{bilayer}}^{\text{inter}} = V \int dx \left\{ \Phi_+^{(1)\dagger}(x) \Phi_+^{(2)}(x-\delta) e^{-i\frac{K_0}{2}\delta} + \Phi_-^{(1)\dagger}(x) \Phi_-^{(2)}(x-\delta) e^{i\frac{K_0}{2}\delta} \right\} + h.c. \quad (\text{S18})$$

We then replace $\partial_y \rightarrow \partial_x$ and $y \rightarrow x - \delta_0$ in equation (S15). The effective basis when working with both layers is given by:

$$\Psi^{\text{bilayer}}(x) = \begin{pmatrix} \Phi_+^{(1)}(x) \\ \Phi_-^{(1)}(x) \\ \Phi_+^{(2)}(x - \delta_0) \\ \Phi_-^{(2)}(x - \delta_0) \end{pmatrix} \quad (\text{S19})$$

for real space and momentum space respectively. The matrix representation of inter-layer coupling Hamiltonian of Eq.(S18) in real space is written as:

$$H_{\text{bilayer}}^{\text{inter}}(x) = \begin{pmatrix} \mathbf{0}_{2 \times 2} & T_0 \\ T_0^\dagger & \mathbf{0}_{2 \times 2} \end{pmatrix}, \quad (\text{S20})$$

with the interlayer coupling matrix

$$T_0 = \begin{pmatrix} V e^{-i \frac{\kappa_0}{2} \delta_0} & 0 \\ 0 & V e^{i \frac{\kappa_0}{2} \delta_0} \end{pmatrix}. \quad (\text{S21})$$

The bilayer Hamiltonian consists of the Hamiltonian of uncoupled layers and the inter-layer coupling Hamiltonian. Using effective Hamiltonians (S16) and the interlayer coupling (S20), we obtain the effective Hamiltonian for the bilayer system:

$$H_{\text{bilayer}} = \begin{pmatrix} H_{\text{single}} & T_0 \\ T_0^\dagger & H_{\text{single}} \end{pmatrix}, \quad (\text{S22})$$

Another form of the bilayer Hamiltonian in momentum space is reported in Ref. [19]. One can show that the two bilayer Hamiltonians are equivalent using a simple transformation of the basis.

Hamiltonian of the moiré bilayer

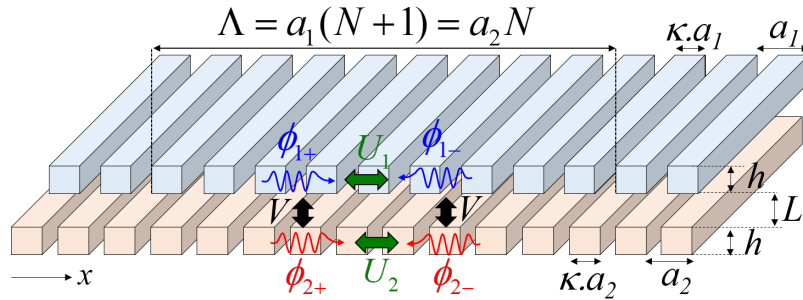


Figure S3. (a) Sketch of a moiré structure.

Hamiltonian of uncoupled layers

We now consider a moiré bilayer of parameters as discussed in the main text (see Fig. S3). With such geometrical design, the Hamiltonian of the uncoupled layers from moiré configuration has the same form as the ones of uncoupled layers as in the bilayer configuration. The only difference to the bilayer configuration is the mismatch between BZ-sizes of the two layers ($K_1 = 2\pi/a_1$ for the upper layer, and $K_2 = 2\pi/a_2$ for the lower layer). The decomposition of wavefunctions corresponding to positive and negative modes is given by:

$$\Phi_{\pm}^{(1)}(x) = \sum_{l \in \mathbb{Z}} e^{\pm i \frac{l K_1}{2} x} \Phi_{l, \pm}^{(1)}(x) = \sum_{l \in \mathbb{Z}} e^{\pm i \frac{l K_1}{2} x} \int_{-\frac{K_1}{4}}^{\frac{K_1}{4}} \frac{dq}{2\pi} \Phi_{l, \pm}^{(1)}(q) e^{i q x}, \quad (\text{S23})$$

$$\Phi_{\pm}^{(2)}(y) = \sum_{l \in \mathbb{Z}} e^{\pm i \frac{lK_2}{2} y} \Phi_{l, \pm}^{(2)}(y) = \sum_{l \in \mathbb{Z}} e^{\pm i \frac{lK_2}{2} y} \int_{-\frac{K_2}{4}}^{\frac{K_2}{4}} \frac{dq}{2\pi} \Phi_{l, \pm}^{(2)}(q) e^{iqy}. \quad (\text{S24})$$

Since the mismatch between BZ-sizes $K_M \ll K_1, K_2$, we expect the interlayer coupling to play an important role when the upper and lower modes are near the symmetry point with the same index l . We consider the effective theory near the symmetry point $l = 1$, and omit the l index by implicitly use $\Phi_{\pm}^{(1)}$ as $\Phi_{1, \pm}^{(1)}$ and $\Phi_{\pm}^{(2)}$ as $\Phi_{1, \pm}^{(2)}$. The basis made of *effective* wave-functions near the crossing point of the positive and the negative bands of each layer

$$\Psi^{(1)}(x) = \begin{pmatrix} \Phi_{+}^{(1)}(x) \\ \Phi_{-}^{(1)}(x) \end{pmatrix}, \quad \Psi^{(2)}(y) = \begin{pmatrix} \Phi_{+}^{(2)}(y) \\ \Phi_{-}^{(2)}(y) \end{pmatrix}. \quad (\text{S25})$$

The Hamiltonian densities of uncoupled layers in these basis are:

$$H_{\text{single}}^{(1)}(x) = \begin{pmatrix} \omega_0^{(1)} - iv^{(1)}\partial_x & U^{(1)} \\ U^{(1)} & \omega_0^{(1)} + iv^{(1)}\partial_x \end{pmatrix}, \quad H_{\text{single}}^{(2)}(y) = \begin{pmatrix} \omega_0^{(2)} - iv^{(2)}\partial_y & U^{(2)} \\ U^{(2)} & \omega_0^{(2)} + iv^{(2)}\partial_y \end{pmatrix}. \quad (\text{S26})$$

The parameters of the Hamiltonians (S26) are determined from the simulation and experiment fitting for a single-layer uni-dimensional photonic crystal slab.

Hamiltonian of inter-layer coupling: moiré configuration

Co-propagating waves of the same momentum but from different layers are coupled via evanescent coupling. The evanescent mechanism is written in term of the coupling Hamiltonian as

$$\mathcal{H}^{\text{inter}} = \int dx \int dy \left[\Phi_{+}^{(1)\dagger}(x) \Phi_{+}^{(2)}(y) \mathcal{V}(x-y) + \Phi_{-}^{(1)\dagger}(x) \Phi_{-}^{(2)}(y) \mathcal{V}(x-y) \right] + h.c. \quad (\text{S27})$$

When $L \ll a$, we can assume that $\mathcal{V}(x-y) = V\delta(x-y-\delta_0)$ where δ_0 is the offset shift between the two layers. Moreover, as discussed in the main text, the value of δ_0 is not relevant for the moiré structure, and we can assume it to be zero. Considering the effective model near the symmetry points corresponding to $l = 1$. We rewrite the inter-coupling Hamiltonian (S27) as the coupling of effective basis $\Phi_{\pm}^{(1)}(x)$ and $\Phi_{\pm}^{(2)}(x)$

$$\begin{aligned} \mathcal{H}^{\text{inter}} &= V \int dx \left[\Phi_{+}^{(1)\dagger}(x) \Phi_{+}^{(2)}(x) e^{-i \frac{(K_1 - K_2)}{2} x} + \Phi_{-}^{(1)\dagger}(x) \Phi_{-}^{(2)}(x) e^{i \frac{(K_1 - K_2)}{2} x} \right] + h.c. \\ &= V \int dx \left[\Phi_{+}^{(1)\dagger}(x) \Phi_{+}^{(2)}(x) e^{-i \frac{K_M}{2} x} + \Phi_{-}^{(1)\dagger}(x) \Phi_{-}^{(2)}(x) e^{i \frac{K_M}{2} x} \right] + h.c. \end{aligned} \quad (\text{S28})$$

Some remarks are in order. We now understand the origin of the spatial dependent phase shift $\phi(x)$ in Eq. (??) in the main text by looking at the expansions (S23) and (S24). Due to the mismatch between BZ-sizes, there is a different phase between the upper and the lower modes near the symmetry points corresponding to the same m . We then choose an effective basis when working with both layers

$$\Psi^{\text{moiré}}(x) = \begin{pmatrix} \Phi_{+}^{(1)}(x) \\ \Phi_{-}^{(1)}(x) \\ \Phi_{+}^{(2)}(x) \\ \Phi_{-}^{(2)}(x) \end{pmatrix} \quad (\text{S29})$$

We then replace $\partial_y \rightarrow \partial_x$ in Eq. (S26) and obtain the matrix representation of the effective Hamiltonian of Eq.(S28) in the effective basis (S29):

$$H_{\text{moiré}}(x) = \begin{pmatrix} H_{\text{single}}^{(1)}(x) & T(x) \\ T^{\dagger}(x) & H_{\text{single}}^{(2)}(x) \end{pmatrix}. \quad (\text{S30})$$

the interlay coupling matrix

$$T(x) = e^{-i \frac{K_M}{2} x} T_1 + e^{i \frac{K_M}{2} x} T_2, \quad T_1 = \begin{pmatrix} V & 0 \\ 0 & 0 \end{pmatrix}, \quad T_2 = \begin{pmatrix} 0 & 0 \\ 0 & V \end{pmatrix} \quad (\text{S31})$$

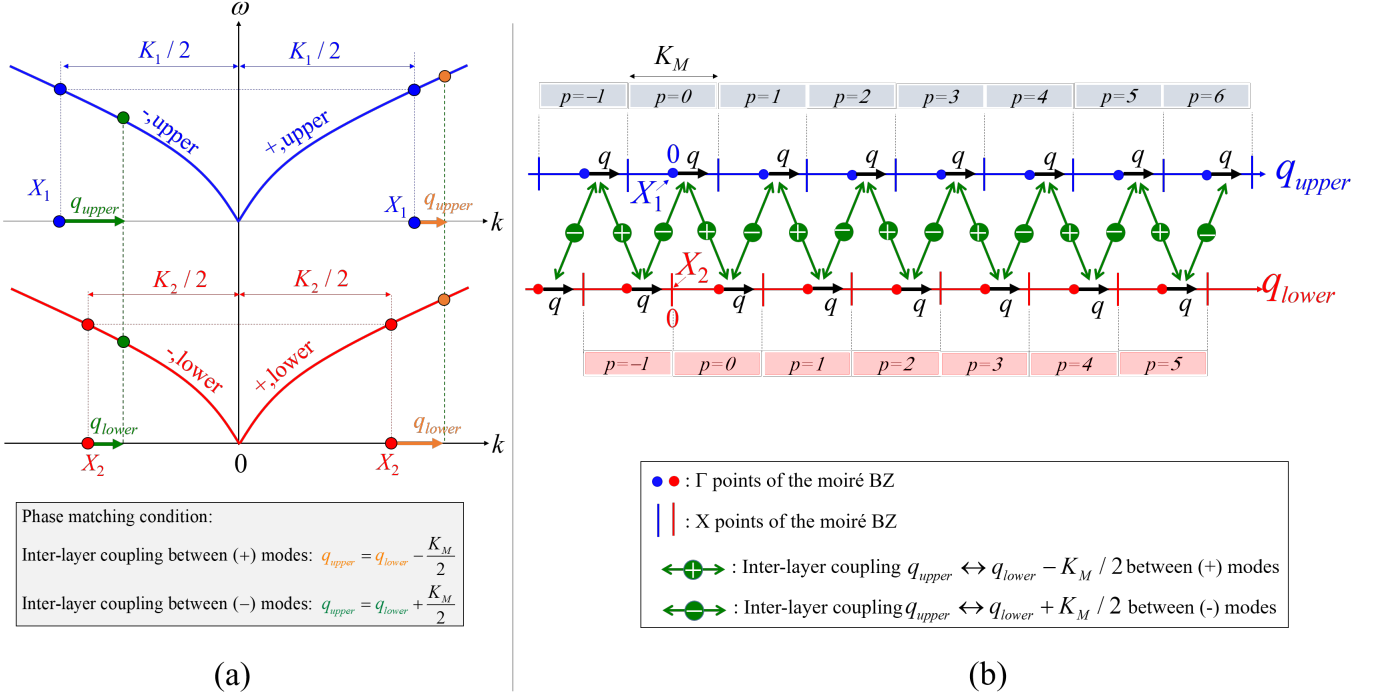


Figure S4. (a)Phase-matching condition (conservation of momentum) for inter-layer coupling between co-propagating waves. (b) Inter-layer coupling mechanism in momentum space between different moiré BZ: Modes in the upper(lower) layer with Bloch momentum q couple to modes in the lower(upper) layer with Bloch momentum $q - \frac{K_M}{2}$ and $q + \frac{K_M}{2}$. Each moiré BZ is indicated by its index p .

The difference of period would lead to a slight difference of values of the offset ω_0 and the intra-layer coupling strength U for each grating and a small modification of V with respect to the case of Bilayer lattice. However, since $\omega_0 \gg U, V$, in the first approximation, only ω_0 varies when switching from upper to lower layer.

The decomposition (S31) shows two types of inter-layer coupling in momentum space:

- The positive mode with effective momentum q in the upper layer will couple to the positive mode with effective momentum $q + \frac{K_M}{2}$ in the lower layer via T_1 .
- The negative mode with effective momentum q in the upper layer will couple to the negative mode with effective momentum $q - \frac{K_M}{2}$ in the lower layer via T_2 .

We demonstrate this coupling mechanism in the momentum space explicitly in Fig S4b. This situation is similar to the inter-layer coupling model suggested by Bistrizer and Mac Donald in twisted bilayer graphene [1]; the only difference is that in twisted bilayer graphene, there are three couplings T_1, T_2 and T_3 corresponding to three momentum shifts instead of just two.

A change of basis:

The effective basis (S29) was chosen in the same manner as in the twisted bilayer graphene literature [2]. Consequently, the Hamiltonian (S30) shares the same pattern as the Hamiltonian derived by Bistrizer and MacDonald in Ref [1, 2] as expected. Notice that in the effective basis (S29), the origins of the effective momenta are different. The wave-function in the coordinate space is given by

$$\Psi(x) = \begin{pmatrix} e^{i\frac{K_1}{2}x} \Phi_+^{(1)}(x) \\ e^{-i\frac{K_1}{2}x} \Phi_-^{(1)}(x) \\ e^{i\frac{K_2}{2}x} \Phi_+^{(2)}(x) \\ e^{-i\frac{K_2}{2}x} \Phi_-^{(2)}(x) \end{pmatrix}. \quad (\text{S32})$$

The wave-function of the electromagnetic wave near the vicinity of X point on the upper layer and lower layer can be read off

from (S32) as

$$\psi^{up}(x) = e^{i\frac{K_1}{2}x}\Phi_+^{(1)}(x) + e^{-i\frac{K_1}{2}x}\Phi_-^{(1)}(x), \quad \psi^{low}(x) = e^{i\frac{K_2}{2}x}\Phi_+^{(2)}(x) + e^{-i\frac{K_2}{2}x}\Phi_-^{(2)}(x). \quad (\text{S33})$$

One can use (S33) solved from effective Hamiltonian (S30) to compare directly with the electromagnetic wave in coordinate space of simulations and experiments. However, it is helpful to introduce another effective basis such that the wavefunction in the coordinate space is

$$\Psi(x) = \begin{pmatrix} e^{i\frac{K_1}{2}x}\Phi_+^{(1)}(x) \\ e^{-i\frac{K_1}{2}x}\Phi_-^{(1)}(x) \\ e^{i\frac{K_2}{2}x}\Phi_+^{(2)}(x) \\ e^{-i\frac{K_2}{2}x}\Phi_-^{(2)}(x) \end{pmatrix} = \begin{pmatrix} e^{i\frac{K_1}{2}x}\Phi_+^{(1)}(x) \\ e^{-i\frac{K_1}{2}x}\Phi_-^{(1)}(x) \\ e^{i\frac{K_1}{2}x}\tilde{\Phi}_+^{(2)}(x) \\ e^{-i\frac{K_1}{2}x}\tilde{\Phi}_-^{(2)}(x) \end{pmatrix}, \quad (\text{S34})$$

which implies

$$\tilde{\Phi}_+^{(2)}(x) = e^{-iK_M x/2}\Phi_+^{(2)}(x), \quad \tilde{\Phi}_-^{(2)}(x) = e^{iK_M x/2}\Phi_-^{(2)}(x). \quad (\text{S35})$$

We are able to rewrite the moiré Hamiltonian (S30) in the new effective basis

$$\tilde{\Psi}^{\text{moiré}}(x) = \begin{pmatrix} \Phi_+^{(1)}(x) \\ \Phi_-^{(1)}(x) \\ \tilde{\Phi}_+^{(2)}(x) \\ \tilde{\Phi}_-^{(2)}(x) \end{pmatrix} \quad (\text{S36})$$

explicitly as follow

$$H = \begin{pmatrix} -v^{(1)}i\partial_x + \omega_0^{(1)} & U^{(1)} & V & 0 \\ U^{(1)} & +v^{(1)}i\partial_x + \omega_0^{(1)} & 0 & V \\ V & 0 & -v^{(2)}i\partial_x + \omega_0^{(2)} & U^{(2)}e^{-iK_M x} \\ 0 & V & U^{(2)}e^{iK_M x} & +v^{(2)}i\partial_x + \omega_0^{(2)} \end{pmatrix}. \quad (\text{S37})$$

Since $K_1 = (N+1)K_M$, the momentum of the effective basis $\Phi_{\pm}^{(1)}(q)$ and $\tilde{\Phi}_{\pm}^{(2)}(q)$ are folded back to the same point in the moiré BZ. Therefore, the new effective basis (S36) is convenient to compare with the moiré wave-functions from simulations and experiments in the momentum space (moiré BZ). The Hamiltonian (S37) is nothing but the effective Hamiltonian (1) in the main text.

Qualitative analysis of the effective Hamiltonian

Dimensional analysis and simplified model

Let us notice that when a time scale (or equivalently energy, or frequency, scale) is fixed, one is still free to choose a length scale in the Hamiltonian (S30). To fix a length scale, one can set $v = 1$. Since one can choose an arbitrary reference value for the energy, clearly the absolute values of $\omega_0^{(1)}$ and $\omega_0^{(2)}$ are not important. It is however crucial that they are different to separate the energy bands of the two uncoupled layers from each other. We thus can substitute $\omega_0^{(1)} \rightarrow \Delta$, $\omega_0^{(2)} \rightarrow -\Delta$ for the qualitative consideration, i.e., choosing the zero-energy to be $\omega_{00} = (\omega_0^{(1)} + \omega_0^{(2)})/2$. Furthermore, let $U = (U^{(1)} + U^{(2)})/2$ and $\Delta_U = (U^{(1)} - U^{(2)})/2$. We then have the simplified Hamiltonian as

$$\begin{aligned} H = & -i\partial_x(\mathbb{I} \otimes \sigma_z) + \Delta(\sigma_z \otimes \mathbb{I}) + U(\mathbb{I} \otimes \sigma_x) \\ & + V(\sigma_+ \otimes e^{-iq_0 x \sigma_z} + \sigma_- \otimes e^{+iq_0 x \sigma_z}) \\ & + \Delta_U \sigma_z \otimes \sigma_x, \end{aligned} \quad (\text{S38})$$

where the characteristic wavevector is $q_0 = K_M/2$ with K_M is the moiré wavevector. Here \otimes denotes the Kronecker product, $\sigma_{x,y,z}$ are Pauli matrices defined by $\sigma_x = \begin{pmatrix} 0 & 1 \\ 1 & 0 \end{pmatrix}$, $\sigma_y = \begin{pmatrix} 0 & -i \\ i & 0 \end{pmatrix}$, $\sigma_z = \begin{pmatrix} 1 & 0 \\ 0 & -1 \end{pmatrix}$, and $\sigma_{\pm} = (\sigma_x \pm i\sigma_y)/2$. The last

term in Hamiltonian (S38) only leads to minor quantitative corrections; for qualitative analysis, one can set $\Delta_U = 0$. We see then that the equation (S38) is characterised by parameters (U, Δ, q_0, V) . All of these quantities have the same dimension of energy (since $v = 1$). One can effectively set one of them, e.g., U , to be the unit.

Moreover, when we specialise to the particular realisation of the effective Hamiltonian (S38), as in Appendix , we see that the parameters $\Delta = \omega^{(1)} - \omega^{(2)}$, $\Delta_U = U^{(1)} - U^{(2)}$ and $q_0 = \frac{K_M}{2}$ are in fact physically dependent through the straining parameter in the system. In this case, we therefore only have three independent physical parameters (U, q_0, V) . The model is specified by two dimensionless ratios between the independent parameters.

Periodicity and the Bloch Hamiltonian

It is perhaps surprising when one notices that the Hamiltonian (S38) seem to be periodic with the double supercell period $2\pi/q_0 = 2\Lambda$, which we refer to as *apparent period*. Accordingly, naively solving these Hamiltonian one obtains a band structure with the *apparent Brillouin zone* of size $K_M/2$. The Hamiltonian is in fact of higher translational symmetry. Indeed, let T_Λ be the translation operator of one moiré period. Then one can easily verify that [45] the Hamiltonian is invariant under the generalized translational operator $T_\Lambda(\sigma_z \otimes \mathbb{I})$. The operator $T_\Lambda(\sigma_z \otimes \mathbb{I})$ generates the commutative group of generalised translational operators, under which the Hamiltonian is invariant. This shows that the *actual period* of the system is, not surprisingly, the moiré period Λ .

With the apparent period of 2Λ , the Bloch theorem states that we can assume the eigenstate of the Hamiltonian (S38) to be of the form

$$\Psi(x) = e^{iqx} u_q(x), \quad (\text{S39})$$

where q is the moiré Bloch vector, $-q_0/2 \leq q \leq +q_0/2$ and the four-spinor $u_q(x)$ is periodic with the apparent period 2Λ . This leads to the Bloch Hamiltonian for $u_q(x)$,

$$H_q = \begin{pmatrix} -i\partial_x + q + \Delta & U^{(1)} & V e^{-iq_0x} & 0 \\ U^{(1)} & +i\partial_x - q + \Delta & 0 & V e^{+iq_0x} \\ V e^{+iq_0x} & 0 & -i\partial_x + q - \Delta & U^{(2)} \\ 0 & V e^{-iq_0x} & U^{(2)} & +i\partial_x - q - \Delta \end{pmatrix}. \quad (\text{S40})$$

This Hamiltonian is to be solved for eigenvalues E_q with periodic eigenstates $u_q(x)$, where the latter is also denoted by $u_{E,q}(x)$ when the explicit energy value is necessary for the clarity. The periodicity of the Bloch wavefunction $u_q(x)$ allows for the solution of the eigenvalue problem to be found through Fourier expansion.

It is important to emphasize again that when using the apparent period 2Λ of the Hamiltonian to calculate the band structure, the Bloch momentum q in equation (S40) is folded within $[-q_0/2, q_0/2]$. In order to unfold the band to the full moiré Brillouin zone $[-q_0, q_0]$, one simply solves the Bloch Hamiltonian for q in the full moiré Brillouin zone, but maintains only solutions that satisfy the generalised Bloch theorem $T_\Lambda(\sigma_z \otimes \mathbb{I})\Psi(x) = e^{iqx}\Psi(x)$. In this way, the unfolded band structure such as in Fig. 2 can be obtained.

Symmetry analysis

Since the moiré system has spatial reflection and time-reversal symmetries, one expects that the Hamiltonian (S38) also carries these symmetries. This is indeed the case:

- **Spatial reflection:** Consider the reflection along the x -axis. Let P denote the pure spatial coordinate reflection operator. Since the reflection of the x -axis also changes the signs of the momenta within each chain, it also exchanges the two basis wavefunctions chosen in Section . Therefore one can expect that the full reflection operator to be $(\mathbb{I} \otimes \sigma_x)P$. One can easily verify that the Hamiltonian (S38) is indeed invariant under this full reflection operator $(\mathbb{I} \otimes \sigma_x)P$. As also expected, the spatial reflection $(\mathbb{I} \otimes \sigma_x)P$ brings the Bloch Hamiltonian H_q in Eq. (S40), to H_{-q} , implying the energy bands are symmetric under reflecting the Bloch wavevector, $E_q = E_{-q}$, and the Bloch wave functions obey $u_{E,q}(x) = u_{E,-q}(-x)$.
- **Time reversal:** Let K be the complex conjugation. One can verify that the Hamiltonian (S38) is invariant under the full time reversal operator $(\mathbb{I} \otimes \sigma_x)K$. Again the time reversal operator brings H_q to H_{-q} , implying the energy bands are symmetric under reflecting the wavevector, $E_q = E_{-q}$, and the Bloch wave functions obey $u_{E,q}(x) = u_{E,-q}^*(x)$.

SOME MORE DETAILS OF THE ANALYSIS OF THE EFFECTIVE HAMILTONIAN: FLATBANDS, LOCALIZATION, TUNNELLING AND BOUND STATES

Fourier transform of the band structure

Being even and periodic with respect to the moiré wavevector $K_M = 2q_0$, an energy band $E(q)$ is completely described by Fourier coefficients $f_p = \frac{1}{2q_0} \int_{-q_0}^{+q_0} dq \cos(p\pi/q_0) E(q)$. Fig. S5 presents the Fourier components f_p of the flat band as indicated in Fig. 2 in the main text, but with slightly different dimensionless parameters as indicated in the caption. It shows that the first coefficients of the Fourier dominate over higher Fourier components, suggesting in an effective tight-binding model, the nearest neighbour coupling dominates. Importantly, higher Fourier coefficients, although small, do not vanish when the first coefficient vanishes (near the flat band). This suggests that the band, although becomes highly flat at the magic coupling, is not *perfectly* flat.

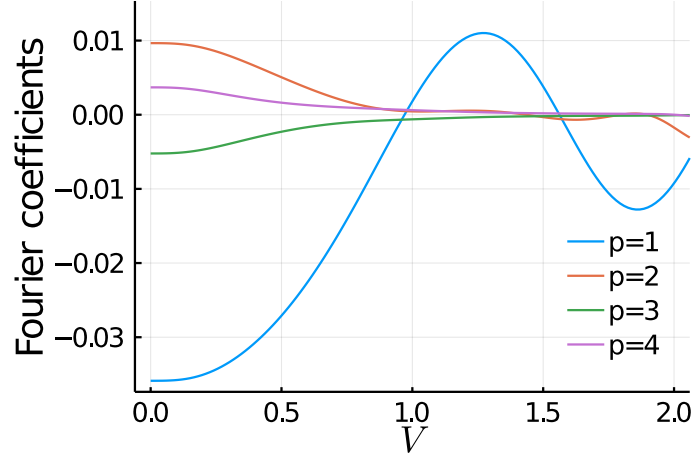


Figure S5. The Fourier coefficients $f_p = \frac{1}{2q_0} \int_{-q_0}^{+q_0} dq \cos(p\pi/q_0) E(q)$ as functions of the couplings V with $U = 1$, $\Delta = -0.3$, $q_0 = 0.6$.

Probability density distribution of the Bloch wave functions and Wannier functions

To study the Bloch wave function near the flat transition, we compute the density

$$\rho(x) = u_q(x)^\dagger u_q(x). \quad (\text{S41})$$

Figure S6 (left) demonstrates the probability densities of the Bloch wavefunctions with varying coupling V across a flat transition. It is important to notice that while the Bloch wave functions tend to concentrate within a moiré period, they do not vanish anywhere (also when the band is flat). In particular, there is no qualitative change in the density of the Bloch wave function as the band is crossing the flat transition.

To consider the possibility of concentrating light in the moiré lattice, we compute the Wannier functions for the Bloch Hamiltonian (S40). The computation of the Wannier function requires fixing the arbitrary phase in the numerical solution of the eigenvectors of the Bloch Hamiltonian (S40). This is a known difficulty in computing Wannier functions with maximal localization [24]. Fortunately, in one-dimensional systems, there is a known gauge fixing procedure, the *twisted parallel transport gauge*, that allows for the computation of Wannier functions of maximal localization [24].

Upon fixing the twisted parallel transport gauge, the Wannier function is then obtained directly as

$$W_0(x) = \frac{1}{2q_0} \int_{-q_0}^{+q_0} dq e^{iqx} u_q(x). \quad (\text{S42})$$

Notice that the integral runs over the full moiré BZ $[-q_0, q_0]$, that is, twice as much of the apparent BZ $[-q_0/2, q_0/2]$. Figure S6 (right) plots the probability density of the Wannier wavefunction (S42). While being highly concentrated, see Fig S7, one should notice that the Wannier function extends beyond a single Moiré period. There is also no qualitative change in the density of the Wannier wave function as the band is crossing the flat transition.

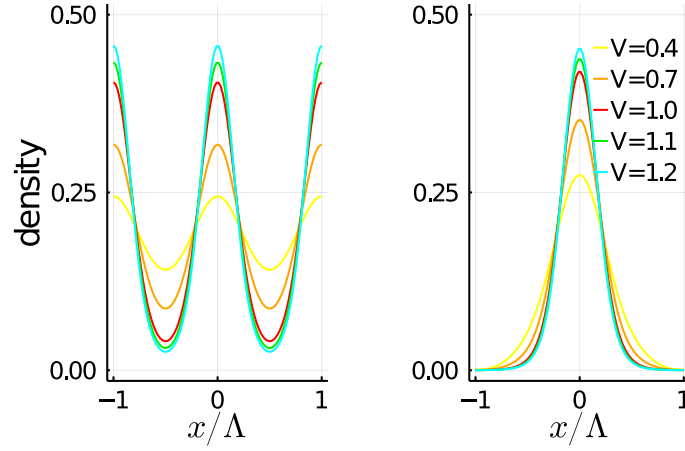


Figure S6. Probability density of the Bloch wavefunction at wavevector $q = 0$ (left) and the Wannier functions (right) of the first positive band with parameters $U = 1$, $\Delta = -0.3$, $q_0 = 0.6$, and varying coupling $V = 0.1, 0.7, 0.9, 1.1, 1.3$ (with $V = 1$ (red) near a flatband transition).

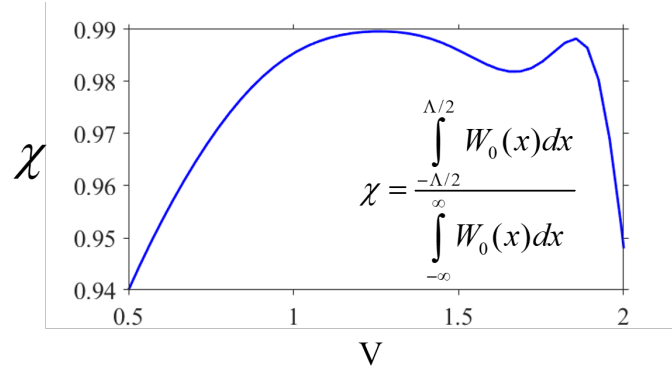


Figure S7. The fraction of Wannier function confined within a moiré period.

Dynamical signature of flatbands

From the above analysis, it is clear that the concentration of the probability density of the Bloch wave function or the Wannier function is not the signature of the flat band. In fact, the very physical meaning of localization in this context is a dynamic one.

Suppose the system has a flatband $u_q(x)$, that is for some energy level $E_q = E_0$, independent of q . Then this is nothing but saying that $\Psi_q(x) = e^{iqx}u_q(x)$ are having the same energy $E_q = E_0$ for all q . This means that given any wave function in momentum space v_q , the wave packet

$$\Psi(x) = \sum_q v_q e^{iqx} u_q(x) \quad (\text{S43})$$

is also an eigen-wavefunction with energy E_0 . As a consequence, the probability density $\Psi(x)^\dagger \Psi(x)$ is unchanged overtime. This is true for any wavepacket v_q in the Bloch momentum space, in particular the Wannier function (S42).

Finite systems: tunnelling and resonances, bound states

To understand better the nature of the flat bands, we compute the tunnelling and bound states of light in a *finite* number of moiré periods. This calculation can be carried out employing the (generalised) transfer matrix method [25], particularly adapted to the case of Dirac-like equations in Ref. [26].

To do so, we rewrite the eigenvalue equation

$$H\Psi(x) = E\Psi(x). \quad (\text{S44})$$

into the form

$$\partial_x \Psi(x) = \mathcal{H}(x)\Psi(x) \quad (\text{S45})$$

where $\mathcal{H}(x)$ is a 4×4 matrix given by

$$\mathcal{H}(x) = i \begin{pmatrix} -(\Delta - E) & -U & -Ve^{-iq_0x} & 0 \\ U & \Delta - E & 0 & Ve^{+iq_0x} \\ -Ve^{+iq_0x} & 0 & -(\Delta - E) & -U \\ 0 & Ve^{-iq_0x} & U & \Delta - E \end{pmatrix}. \quad (\text{S46})$$

All possible x -evolutions of the x -dynamical equation (S45) is described by the 4×4 x -evolution operator $G_E(x_2, x_1)$, which is the solution of

$$\partial_{x_2} G_E(x_2, x_1) = \mathcal{H}(x_2)G_E(x_2, x_1), \quad (\text{S47})$$

subject to the initial condition $G_E(x_2, x_1) = \mathbb{I}$.

The function $G_E(x_2, x_1)$ summarises *all* information about the eigenwave function $\Psi(x)$ corresponding to the eigenvalue E of the Hamiltonian H . Therefore it is a convenient way to relate different properties of H , such as the existence of extended states, transmission amplitudes, probability distribution, the density of states, etc. On the other hand, with well-developed methods for the ordinary differential equations (ODEs) [46], the computation of $G_E(x_2, x_1)$ is relatively easy. One should, however, notice that the x -dynamics is non-hermitian and sometimes numerical instabilities have to be addressed.

Boundary condition and the computation of tunnelling rate

To investigate the tunnelling phenomena through the finite moiré structure between x_1 and x_2 , one has to consider the realisation of the asymptotic area outside the moiré structure. For convenience, we choose this to be of the type of fishbone structure [19]; that is, fixing the phase in the coupling between the two chains in the Hamiltonian (S38) to be $e^{\pm iq_0x_1}$ (constant) for $x \leq x_1$, and $e^{\pm iq_0x_2}$ (constant) for $x \geq x_2$.

For the fixed phases $e^{\pm iq_0x_1}$ or $e^{\pm iq_0x_2}$, the eigenstate of the Hamiltonian (S38) can be easily solved, resulted in the fishbone band structure [19]. Plugging a plane-wave solution Ce^{ikx} into the resulted Hamiltonian, one finds the fishbone eigenvalue equation,

$$\begin{pmatrix} k + \Delta - E & U & Ve^{-i\phi} & 0 \\ U & -k + \Delta - E & 0 & Ve^{+i\phi} \\ Ve^{+i\phi} & 0 & k - \Delta - E & U \\ 0 & Ve^{-i\phi} & U & -k - \Delta - E \end{pmatrix} C = 0, \quad (\text{S48})$$

where $\phi = q_0x_1$ or $\phi = q_0x_2$, which are here simply constants. Fixing the energy E , we are interested in solving this equation for k . The resulted equation is a generalised eigenvalue problem. In general, the obtained generalised eigenvalues k are complex. To fix an ordering, we order the four (generalised) eigenvalues k according to their increasing phases, that is, the angles with respect to the real axis, computed counterclockwise.

Let us consider the possible solutions of equation (S48). One sees that if k is a solution, k^* is also a solution (time-reversal symmetry). Also, if k is a solution, $-k$ is also a solution (spatial reflection symmetry). In general, one has 4 different wavevectors satisfying (S48). If one of the solution k is generically complex (i.e., not pure real or pure imaginary), then by acting with the time-reversal symmetry and reflection symmetry, one obtains all the other three solutions k^* , $-k$, $-k^*$, which are also generically complex. On the other hand, if one of the solution k is real, then the time-reversal symmetry and the reflection symmetry only give $-k$ as another solution. There are then two possibilities: the other two solutions can also be real, or they must be purely imaginary.

To consider the tunnelling phenomena, we are interested in the energy range of $+\Delta + U \leq E \leq -\Delta + U$ (for $\Delta < 0$). Here for a fixed energy E , there are two real wavevectors $\pm k$ (with the convention $k \geq 0$), corresponding to the phases of 0 and π . Two other modes are of pure imaginary wavevectors $i\kappa$ (with the convention $\kappa \geq 0$) corresponding to exponential decaying or exponential amplifying modes and phases of $\pi/2$ and $3\pi/2$. By W we denote the matrix of which the columns

are the corresponding eigenvectors (ordered such that phases of the eigenvalues increase, here must be $0, \pi/2, \pi$ and $3\pi/2$). The general wavefunction depends on 4 amplitudes of these different solutions, a^\pm and b^\pm , explicitly given by

$$\Psi(x) = WV(x) \begin{pmatrix} a^+ \\ b^+ \\ a^- \\ b^- \end{pmatrix} \quad (\text{S49})$$

where

$$V(x) = \begin{pmatrix} e^{ikx} & 0 & 0 & 0 \\ 0 & e^{-\kappa x} & 0 & 0 \\ 0 & 0 & e^{-ikx} & 0 \\ 0 & 0 & 0 & e^{+\kappa x} \end{pmatrix}. \quad (\text{S50})$$

According to the ordering convention, a^\pm are the amplitudes of the travelling modes (corresponding to phases of eigenvalues k of 0 and π) and b^\pm are the amplitudes of the exponential modes (corresponding to phases of the eigenvalues k of $\pi/2$ and $3\pi/2$).

This solution can be applied to both the areas $x \leq x_1$ and $x \geq x_2$ with corresponding amplitudes a_1^\pm and b_1^\pm and a_2^\pm and b_2^\pm . This results in the wave function at $x = x_1$ to be $\Psi(x_1) = W_1 V_1(x_1)(a_1^+, b_1^+, a_1^-, b_1^-)^T$ and at $x = x_2$ to be $\Psi(x_2) = W_2 V_2(x_2)(a_2^+, b_2^+, a_2^-, b_2^-)^T$. Now using the solution of the wavefunction $G(x_2, x_1)$ through the moiré periods as obtained from the generalised transfer matrix, $\Psi(x_2) = G(x_2, x_1)\Psi(x_1)$, one obtains

$$\mathcal{T} \begin{pmatrix} a_1^+ \\ b_1^+ \\ a_1^- \\ b_1^- \end{pmatrix} = \begin{pmatrix} a_2^+ \\ b_2^+ \\ a_2^- \\ b_2^- \end{pmatrix} \quad (\text{S51})$$

where the *transfer matrix* \mathcal{T} is given by

$$\mathcal{T} = V_2(x_2)^{-1} W_2^{-1} G(x_2, x_1) W_1 V_1(x_1). \quad (\text{S52})$$

To obtain the tunnelling rate, we apply the boundary condition $(a_1^+, b_1^+, a_1^-, b_1^-) = (1, 0, r, l_1)$ and $(a_2^+, b_2^+, a_2^-, b_2^-) = (t, l_2, 0, 0)$. It is interesting to notice that the exponential modes also participate in the process: by injecting a plane wave at $a_1^+ = 1$, a wave is reflected at $a_1^- = r$, some part $a_2^+ = t$ is transmitted though; and at the same time the (left and right) exponentially decaying modes are excited with amplitudes l_1 and l_2 . This gives rise to the formula for the reflection coefficients and transmission coefficients as

$$r = -\frac{\mathcal{T}_{44}\mathcal{T}_{31} - \mathcal{T}_{34}\mathcal{T}_{41}}{\mathcal{T}_{33}\mathcal{T}_{44} - \mathcal{T}_{34}\mathcal{T}_{43}} \quad (\text{S53})$$

$$l_1 = -\frac{-\mathcal{T}_{43}\mathcal{T}_{31} + \mathcal{T}_{33}\mathcal{T}_{41}}{\mathcal{T}_{33}\mathcal{T}_{44} - \mathcal{T}_{34}\mathcal{T}_{43}} \quad (\text{S54})$$

$$t = \mathcal{T}_{11} + r\mathcal{T}_{12} + l_1\mathcal{T}_{14}. \quad (\text{S55})$$

Obtaining the transmission coefficients, one can exact its resonant structure, which indicates the quasi-bound states of light in the system. These obtained quasi-bound states can be compared to the band structure of the system of an infinite number of periods. However, it is even more convenient to study the exact bound states in a system of a finite number of moiré periods for our consideration.

Boundary condition and the computation of bound states

As for bound states, we consider again the asymptotic areas to be of fishbone type, but now at $x_1 = \Lambda/2$ and $x_2 = \Lambda/2 + p\Lambda$ for a integer number p . In this scenario, in the energy interval $U + \Delta \leq E \leq U - \Delta$ (notice again that $\Delta < 0$), there is no extended states in the fishbone areas; all four wavevectors as solutions of (S48) are generically complex. Recall that we order the eigenvalues according to their angles with the real axis. To have a bound state, we apply the boundary condition for the amplitudes $(0, 0, l_1, l_2)$ on the left and the amplitudes $(l_3, l_4, 0, 0)$; in either side, only exponentially decaying modes are allowed. This results in the equation to be solved for the energy of the bound states as

$$\mathcal{T}_{34}\mathcal{T}_{43} = \mathcal{T}_{33}\mathcal{T}_{44}. \quad (\text{S56})$$

Using this procedure, we compute the bound states that are supported in a system of two moiré periods, which is presented as a function of the inter-chain coupling V in Fig. S8. One observes that flat band transitions happen very close to the degenerate point of the two bound states of the system of two moiré periods.

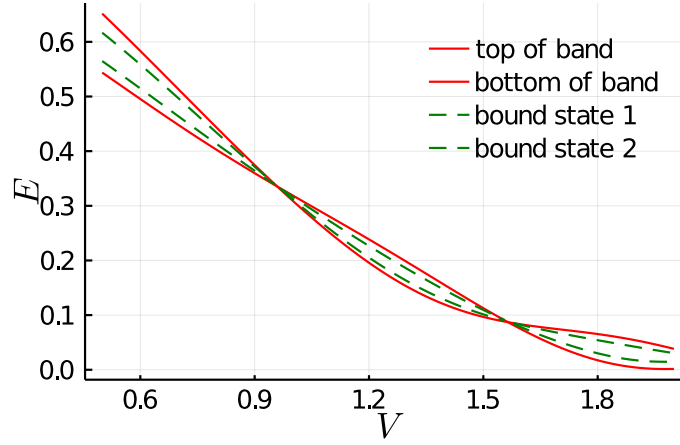


Figure S8. Comparison of bound states of two moiré periods with the top and the bottom of the lowest positive band of the periodic system. Flat bands happen close to the degenerate point of the two bound states of the system of two moiré periods. Here $U = 1$, $\Delta = -0.3$, $q_0 = 0.6$.

Derivation of the band structure of the infinite system

As an interesting side remark, we mention that the band structure of the system can also be computed from the generalised transfer matrix $G(x_2, x_1)$. To this end, we choose $x_2 - x_1$ to be an apparent period of the potential (twice as much of the moiré period), $x_2 - x_1 = 2\Lambda$. Then from the fact that $\Psi(x_2) = G(x_2, x_1)\Psi(x_1)$ and the Bloch theorem $\Psi(x_2) = e^{iq2\Lambda}\Psi(x_1)$ we obtain $\det[G(x_2, x_1) - e^{iq2\Lambda}] = 0$. This allows one to compute the Bloch wavevector corresponding to the energy under consideration E . By selecting the real wave vector q , the band structure of the system can then be derived.

PARAMETER RETRIEVAL FOR THE EFFECTIVE HAMILTONIANS

The effective Hamiltonian of the moiré structure is determined by the energies $\omega_0^{(1,2)}$, $U^{(1,2)}$, V and the group velocity v . These values are retrieved from the dispersion characteristics of the single layer structure (for ω_0, U and v), and of the bilayer structure (for V) which are obtained by RCWA simulations. In the following, we will discuss in details these parameter retrieval methods.

Parameter retrieval of single grating structure

The dispersion characteristic of a single grating structure is easily calculated from Eq. (S14) in the main text. It consists of two bands of opposite curvature $\pm \frac{v^2}{2U}$, with corresponding band edge energies given by $\omega_0 \pm U$. As a consequence, ω_0 and U are directly extracted from the energy of resonances at $q = 0$ of the RCWA simulations. Then knowing U , the group velocity v is extracted from the curvature of these resonance. As shown in Fig. S9b, the band structure which is calculated by the effective Hamiltonian using the retrieved parameters reproduce perfectly the simulated one.

With the retrieval method presented above, we can explore the dependence of U , ω_0 and v on geometrical parameters of the system. In particular, two dependencies are studied in details:

- **Dependence on the period a when a is slightly different than a_0 :** this dependence is responsible to the slight difference between $U^{(1)}, \omega_0^{(1)}$ and $U^{(2)}, \omega_0^{(2)}$ corresponding to upper and lower gratings of period a_1 and a_2 . The results of this study are shown in Fig. S9c. We notice that the linear dependence $\omega_0(a)$ leading to a simple proportional relation between $\Delta = \frac{\omega_0^{(1)} - \omega_0^{(2)}}{2}$, $\Delta_U = \frac{U^{(1)} - U^{(2)}}{2}$ and $\frac{1}{N} \approx \frac{a_2 - a_1}{a_0}$. As a consequence, the three parameters Δ, Δ_U and q_0 of the Hamiltonian (S38) are connected and can be reduced to a single one, for example q_0 .
- **Dependence on the filling fraction κ :** the strong and almost linear dependence of $U(\kappa)$ is shown in Fig. S9d. It suggests that the filling fraction is the parameter for tuning the intralayer coupling strength.

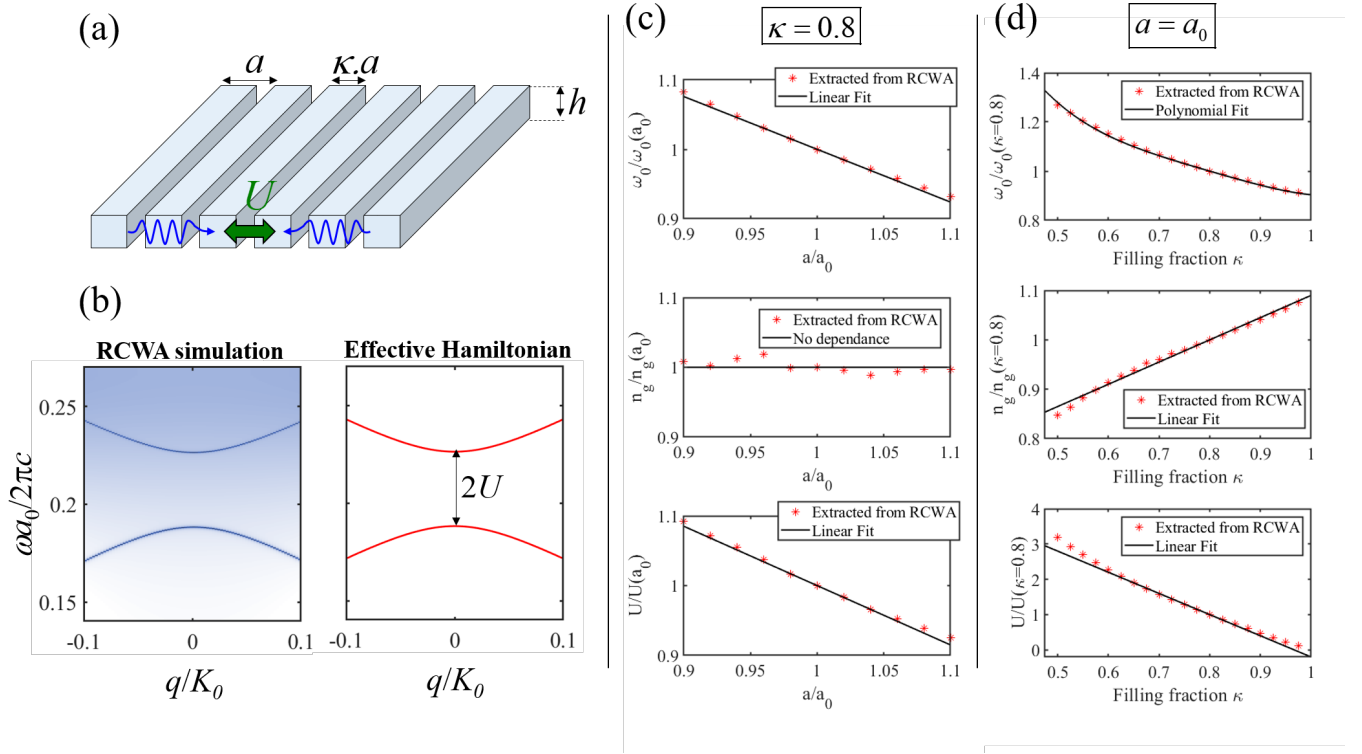


Figure S9. (a) Sketch of a single grating structure. (b) Band structure of a single grating structure obtained by RCWA simulation (left) and by the effective Hamiltonian using retrieved parameter U , ω_0 , v . Here the simulated structure corresponds to $a = a_0$, $\kappa = 0.8$ and $h = 0.6a_0$. The retrieved parameters are $\omega_0 = \Omega_0$, $U = U_0$ and $n_g = c/v = 3$. With $\Omega_0 a_0 / 2\pi c = 0.2073$ and $U_0 a_0 / 2\pi c = 0.0191$. (c) Dependence of the retrieved parameters when the period a is slightly different than a_0 . It shows that the group velocity v is almost unchanged, while ω_0 and U are slightly modified. The modifications of ω_0 and U can be fitted by $\omega_0(a) = \Omega_0 [1 - 0.76 (a/a_0 - 1)]$ and $U(a) = U_0 [1 - 0.85 (a/a_0 - 1)]$. (d) Dependence of the retrieved parameters when the filling fraction κ is scanned from 0.5 to 1. It shows that while the offset energy ω_0 and the group velocity are slightly modified, the intra-layer coupling strength U is greatly modified from $3U_0$ to 0.

Parameter retrieval of bilayer structure

The dispersion characteristic of bilayer structure can be analytically calculated from Eq. (S22) from the main text. The detailed of these eigenmodes has been reported in [19]. Here we only discuss how to retrieve the inter-layer coupling strength from these band structure and the validation of the method.

Since ω_0 and U are already retrieved from the simulation of single grating, only V left to be retrieved. One may show that, for AA stacking (i.e. $\delta/a = 0$), the band structure consist of four bands with bandedge energies given by $\omega_0 \pm U + V$ and $\omega_0 \pm -V$. As a consequence, V is directly extracted from the energy of resonance at $q = 0$ of the RCWA simulations for anyone from the four bands. Using this method, we can easily obtain the dependence of V as the function of the distance L separating the two grating. The results shown in Fig. S10b evidences the dependence law $V = V_0 e^{-L/L_0}$ used in the main text.

Finally, we confirm the validity of the retrieved parameters by using them to calculate the band structure of the bilayer for different relative shift δ/a , and for different value of L . The results presented in Fig. S10c show perfect agreement between the calculated dispersion and the ones obtained by RCWA simulations, thus validate the retrieved parameters.

BAND EDGES OF MOIRÉ BANDS

To investigate the interplay between intra and inter-layer coupling in the formation of moiré bands, the band-edge energies (at Γ and X points) of electron-like and hole-like moiré bands are extracted from effective Hamiltonian calculations when scanning

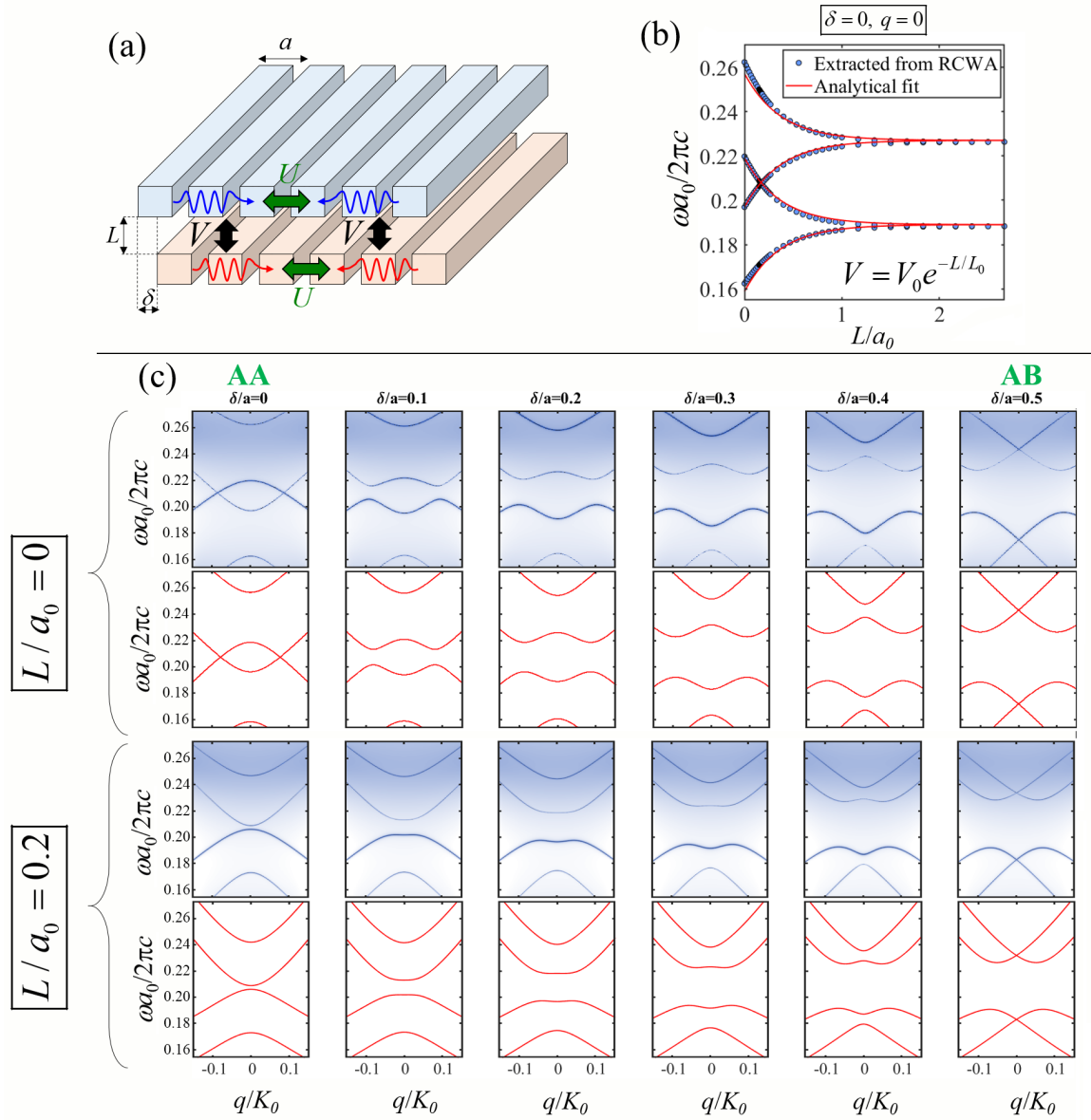


Figure S10. (a) Sketch of a bilayer grating structure. (b) Band-edge energies of the band structure of a bilayer grating as a function of the distance L between the two layers. The two gratings are identical and aligned, with $a = a_0$, $\kappa = 0.8$ and $h = 0.6a_0$. The blue circles correspond to extracted data from RCWA simulation. The solid red lines are fittings, given by $\omega_0 \pm U - V$ and $\omega_0 \pm U + V$. Here $\omega_0 = \Omega_0$ and $U = U_0$, obtained from parameter retrieval of the single grating. And $V(L) = V_0 e^{-L/L_0}$ with $V_0 a_0 / 2\pi c = 0.032$ and $L_0 / a_0 = 0.34$. (c) Band structure of bilayer grating structures of different relative displacement δ/a , obtained by RCWA simulation and by the effective Hamiltonian using retrieved parameter U, ω_0, v and V .

the ratio V/U for different moiré configurations with fixed value of $U = U_0$. The results depicted in Fig S11 evidence two important features:

- The magic configuration takes place at the crossings of band edge energies from the same miniband when tuning V/U (indicated by green arrows in Figs S11).
- The two moiré bands get closer when increasing V/U , as previously discussed when scanning L in the maintext. Interestingly, the gap between them is closed, and they merge together when $V/U \gtrsim 2$ for all value of N . Indeed, the bandgap when the two gratings are slightly different (i.e. $N \gg 1$) and uncoupled (i.e. $V \ll U$) is given by the gap of a single grating, thus amounts to $2U$. When the interlayer layer coupling V is implemented, the two moirés bands emerge and are separated to the corresponding continuum by a quantity $\sim V$. Thus they would merge at the zero energy when $V \sim U$.

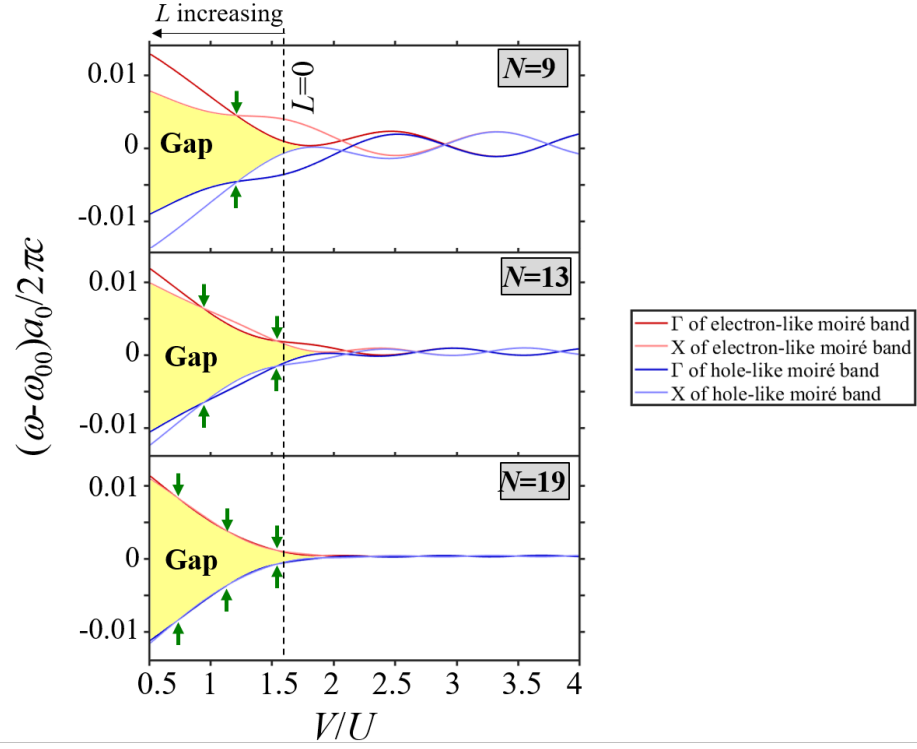


Figure S11. Results from the effective Hamiltonian of the band-edge energies (at Γ and X points of electron-like and hole-like moiré band) when scanning V/U for different moiré structures. The vertical black dashed line indicates the value of V/U corresponding to $L = 0$. The green arrows indicate flat band configurations.

This feature is not revealed from the numerical simulation since the maximum value of V/U from our design is 1.76 (i.e. $L = 0$ and $\kappa = 0.8$).